A Study of Two-Dimensional Materials

A thesis submitted in partial fulfilment for the degree of

Master of Science

as a part of the

Integrated Ph.D. Program (Chemical Science)

by

Amit

New Chemistry Unit

Jawaharlal Nehru Centre For Advanced Scientific Research

(A Deemed University)

Jakkur P.O., Bengaluru-560064

India

March 2019

To

Everyone

Who Believes In Me

DECLARATION

I hereby declare that the matter embodied in this thesis entitled **"A Study of Two-Dimensional Materials"** is the result of investigations carried out by me under the supervision of Prof. C. N. R. Rao, FRS at the New Chemistry Unit, Jawaharlal Nehru Centre for Advanced Scientific Research, Bengaluru, India and that it has not been submitted elsewhere for the award of any degree or diploma.

In keeping with the general practice in reporting scientific observations, due acknowledgement has been made whenever the work described is based on the findings of other investigators. Any omission that might have occurred by oversight or error of judgement is regretted.

Amit

CERTIFICATE

I hereby declare that the matter in the thesis entitled **"A Study of Two-Dimensional Materials"** has been carried out by Mr. Amit at New Chemistry Unit, Jawaharlal Nehru Centre for Advanced Scientific Research, Bengaluru, India under my supervision and that it has not been submitted to elsewhere for the award of any degree or diploma.

Prof. C. N. R. Rao

(Research Supervisor)

ACKNOWLEDGMENTS

To begin with and preeminent, I express my deepest gratitude and profound respect to my research supervisor ***Prof. C. N. R. Rao, FRS***, for presenting me to the interesting areas of atomic layer deposition and two dimensional layered materials. His enthusiasm, dedication and relentless pursuit of science are truly motivating and propelling. I shall remain ever indebted to him for bearing with me throughout the course of the work. I consider myself greatly fortunate to receive all the love and care that he has bestowed me with. He taught me that how to handle challenges in the easiest way. He has been instrumental in shaping my research, my career and my perspective towards life as a whole.

I thank Prof. Aninda J. Bhattacharyya, Prof. Ranjan Datta, Dr. Farheen N. Sayed and Ms. Usha Bhat for their fruitful scientific collaborations and all their insightful discussions.

Special thanks to all my co-workers without their help my work would have been incomplete: Dr. Pramoda, Dr. Sreedhara, Dr. Manjunath, Dr. Gupta, Dr. Chhetri Mr. Monis, Mr. Navin, Mr. Reetendra.

I also take opportunity to thank all my past and present labmates: Dr. Kumar, Dr. Dey, Dr. Sreedhara, Dr. Manjunath, Dr. Gopal, Dr. Pramoda, Dr. Lingampalli, Dr. Jana, Dr. Vishnoi, Dr. Gupta, Dr. Chhetri, Mr. Roy, Mr. Manjunatha, Mr. Rajesh, Ms. Manaswee, Mr. Monis, Mr. Navin, Mr. Rohit, Mr. Swaraj and Mr. Reetendra.

I especially thanks Mr. Monis and Ms. Manaswee, for the valuable discussions and support I got from them.

I thank my course work instructors: Prof. S. J. George, Prof. R. Viswanatha, Prof. J. Haldar, Prof. K. Biswas, Prof. S. C. Peter, Prof. H. Ila, Dr. S. Agasti, Dr.

Premkumar, Prof. S. Balasubramanian, Prof. A. Sundersan, Prof. Eswaramoorthy, Prof. S. Rajaram, Prof. S. Narasimhan, Prof. T. K. Maji for the excellent course work.

My sincere thanks to the technical staff Ms. Selvi, Mrs. T. Usha, Mr. Vasu, Mr. Anil, Mr. Srinath, Dr. Joy, Mr. Kannan, Mr. Jagadish and Mr. Shivkumar. I thank Mrs. Sudha, Mrs. Shashi, Mrs. Ramya, Mr. Gowda, Mr. Victor, Ms. Shweta, Ms. Melissa, Mr. Naveen for their help in various aspects. I extended my thanks to Hostel, Admin, Academic, Library, Dining hall and Dhanvantri and other departmental staff for all their help.

I am thankful to JNCASR for financial support and fellowship.

I take this opportunity to thank Mrs. Indumati Rao for all the affection and love I have received from her. Her enthusiasm has been a source of inspiration for me.. I take this opportunity to thank Mr. Sanjay Rao for his hospitality.

My sincere thanks to all my batchmates Aditi, Geetika, Harshit, Sushmita, Ashutosh, Brijesh, Nijita, Pragya, Ragya, Shashank, Shivani, Tarndeep, Ankit Chavi, Irine, Kuldeep, Rashi, Shubham, Saheli.

My special thanks to the teachers at my school (J.N.V., Butana) and college (Sri Venkateswara College, New Delhi).

I am thankful to my friends Saurabh, Vikas, Aditi, Anamika who were with me in hard times.

I thank all my juniors and seniors, whose list of names is too long, but who nevertheless, have inspired me, at some moment through personal interactions.

Finally and most importantly, I am grateful to my family, especially my parents, brothers Ravi, Ashish, Rahul, Rohit and Sister Tannu for their love, support and constant encouragement throughout the my life.

PREFACE

The thesis contains results of investigations carried out on the 2D layered materials such as PbFCl, MoS_2, $MoSe_2$, BCN, BN, C_3N_4 their properties and photochemical hydrogen evolution activity of various cross-linked 2D layered structures. It also contains report on TiS_2 thin films grown by atomic layer deposition (ALD) and their applications in Li/Na-ion batteries.

It contains the following chapters:

Chapter 1: A study of two-dimensional PbFCl

Chapter 2: Covalently-linked 2H-MoS_2 and $MoSe_2$ with other 2D layered materials and stable the 1T-forms by hydrothermal and solvothermal methods, showing remarkable photochemical HER activity

Chapter 3: Atomic Layer Deposition of TiS_2-Nanowall Networks with Superior Performance in Thin Film Rechargeable Batteries

TABLE OF CONTENTS

CHAPTER 1

A study of two-dimensional PbFCl

SUMMARY

In recent times two dimensional layered materials emerged as an active area of research. While materials like graphene, MoS_2, borocarbonitride have been investigated thoroughly, there are numerous other layered materials which are yet to be explored. One such example is PbFCl. In this work we have synthesized PbFCl by solid state synthesis and exfoliated in various solvents by liquid exfoliation. The compound was subjected to various characterization techniques. We have studied the effect of intercalation of various solvents on layered structure of PbFCl.

Introduction

Two-dimensional materials have gained great importance ever since the discovery of graphene.[1–5] A variety of 2D materials with interesting properties have been discovered, MoS_2 being important one.[6–8] A recent survey[9] has shown there are several hundred inorganic 2D materials, most of them yet to be fully investigated. A simple inorganic 2D material is PbFCl. It occurs naturally as Matlockite, named after a town in Derbyshire, England. It crystallizes in PbFCl-type tetragonal structure having space group P4/nmm. There are large number of compounds which has PbFCl-type structure like PbFBr, PbFI, BaFCl, BaFBr, SrFCl, SrFBr, CaFCl, CaFBr etc.[10] The structure of PbFCl formed by layers parallel to (001) each occupied by a single kind of ion. There are reports on its structure[10–12] but its properties have not been explored. We have been able to prepare single to few layered sheets of PbFCl by exfoliation through ultrasonication. We have studied the properties of the layered sheets of PbFCl and also the intercalation of molecules in the bulk solid.

Experimental

Synthesis

PbFCl was prepared from lead chloride ($PbCl_2$) and ammonium fluoride (NH_4F) by solid state synthesis. In the synthesis procedure, $PbCl_2$ was mixed with an excess of NH_4F and the mixture was heated under continuous flow of nitrogen at 400 °C for 5 hours in an alumina boat, with heating and cooling rate 5 °C/minute. A white powder was collected which was further characterized using microscopic and spectroscopic techniques.

Exfoliation of PbFCl

Mono and few layers of PbFCl were prepared by the liquid exfoliation of PbFCl bulk form in water (1:1 ratio of bulk PbFCl and water) subjecting to probe sonication (750 W and 20 kHz) for 5 hours. Exfoliated nanosheets were separated from the bulk by the centrifugation at 5000 rpm for 5 minutes. The top 50% supernatant solution mixture containing few-layers was collected and used for further characterization. The same procedure was used for exfoliation in ethanol, dimethylformamide (DMF) and N-methyl-2-pyrrolidone (NMP), with sonication for 10 hours.

Intercalation of PbFCl

Intercalation reactions of PbFCl were carried out from the exfoliated PbFCl in which 10 mg of exfoliated material was dispersed in 10 mL of hexane followed by continuous stirring for a period of 24 hours. The precipitate formed was collected by centrifugation, dried and the intercalation were confirmed by XRD and FTIR. The same procedure was used for the intercalation of PbFCl with ethyl methyl ether, pentadecane, CTAB (surfactant) and 1-ethyl-3-methyl imidazolium tetrafluoroborate (ionic liquid).

Characterization

Powder X-ray diffraction (PXRD) data were collected with a Bruker diffractometer (Cu Kα (λ = 1.5406 Å) X-ray source). Fourier-transform infrared (FTIR) spectra were recorded with Bruker IFS 66 v/S spectrometer. Scanning electron microscope (SEM) images were obtained with FEI Nova Nano SEM 600 microscope. Optical transmission spectra were recorded on a PerkinElmer UV-Vis spectrometer and Raman spectra with a Jobin Yvon LabRam HR spectrometer using Ar-laser (λ = 514.5 nm). Transmission electron microscope

(TEM) images were recorded with a FEI Tecnai microscope, operating at 200 kV accelerating voltage. The surface topography were determined by using atomic force microscopy (AFM) in contact mode using Bruker Innova. High-resolution TEM (HRTEM) images were obtained with FEI Titan aberration- corrected electron microscopy. X-ray photoelectron spectra (XPS) were obtained with an Omicron spectrometer using Al Kα as the X-ray source (1486.6 eV).

Hansen solubility parameters

Hansen solubility parameters (HSPs)[13,14] indicates the molecular interactions and efficiently predict and/or examine the dispersibility, solubility, wettability of two different materials. HSPs mainly consist of three terms which arises out of corresponding molecular interactions these are as follows:

1. δd (London dispersion term)
2. δp (polar term)
3. δh (hydrogen bonding term)

These three parameters represents the co-ordinates of a point in three dimensions also known as the Hansen space. Lesser the distance between two molecules are in this three-dimensional space, the more likely they are to dissolve into each other. The units of solubility parameters are $MPa^{1/2}$. The compatibility of two different materials with the respective HSPs of [δd_1, δp_1, δh_1] and [δd_2, δp_2, δh_2]) can be estimated by the HSP distance (Ra) according to the equation:

$$Ra^2 = 4(\delta d_1-\delta d_2)^2 + (\delta p_1-\delta p_2)^2 + (\delta h_1-\delta h_2)^2$$

The HSP Distance between two molecules (Ra) is the measure of how alike they are. The smaller Ra, the more likely they are to be compatible. The HSPs of common solvents are already known, the HSP values, molar volume, surface tension of the probe liquids employed in this study were obtained from the official HSP database.[15]

Results and discussion

The powder diffraction pattern (**Figure** 1) of PbFCl shows that it crystallizes in the tetragonal structure (JCPDS no. 4-460) with the lattice parameters a = 4.106 Å, and c = 7.23 Å and space group is *P4/nmm* (no.129), in agreement with the calculated.[16] The crystal system shows that each Pb is coordinated with 3F and 2Cl atoms with the chlorine atoms occupying the surface in each layer. The bond distances of Pb-F/Cl vary between 2.53 and 2.308 Å. The occupation of Pb, F and Cl atoms in a layer is shown in **Figure** 2.

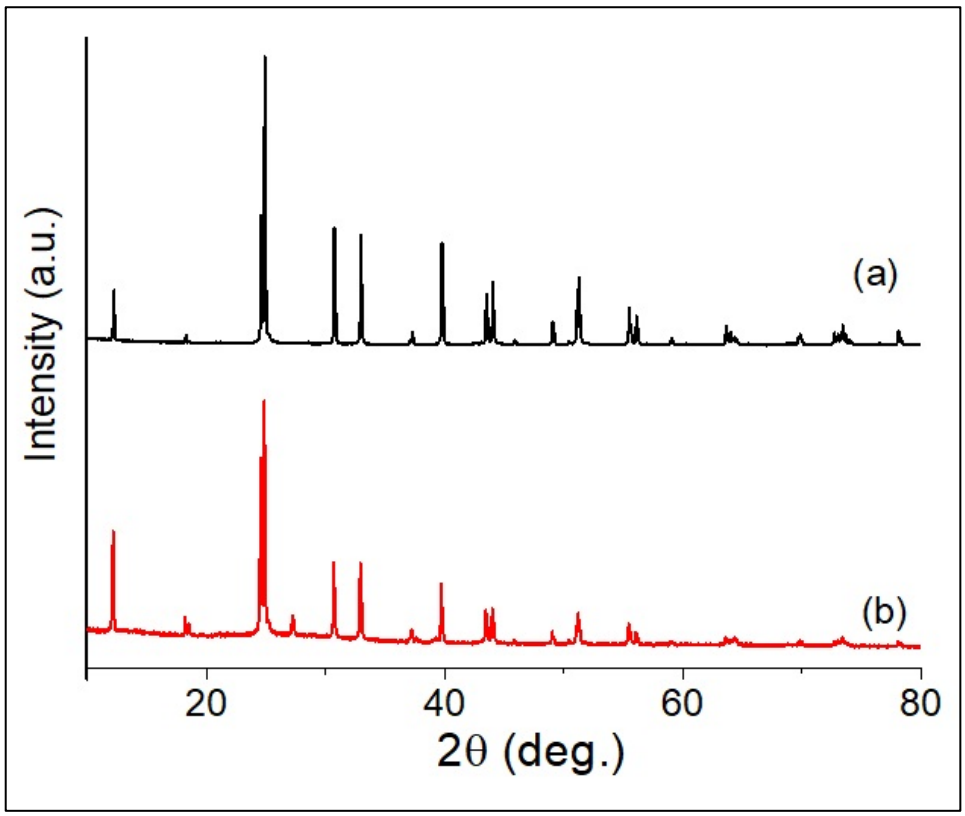

Figure 1: XRD pattern of (a) PbFCl (b) PbFCl exfoliated in water.

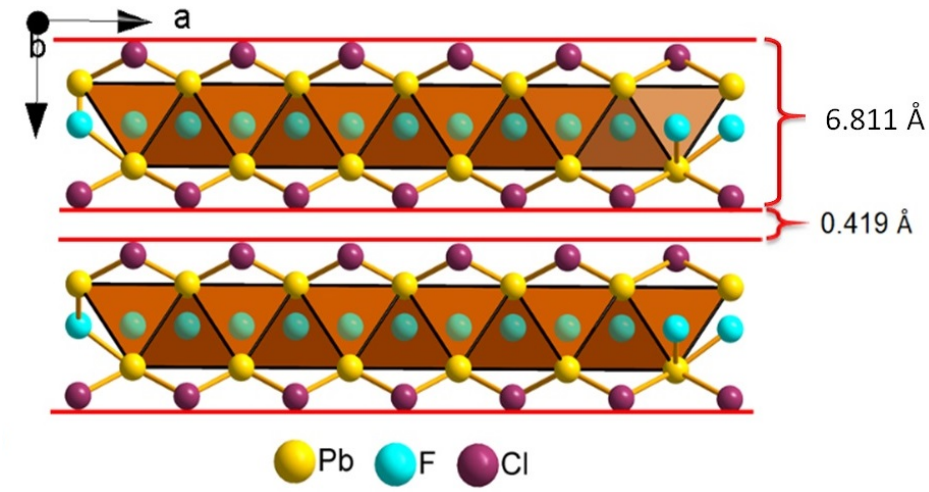

Figure 2: Polyhedral structure of layerd PbFCl.

X-ray photoelectron spectra of PbFCl are shown in **Figure** 3. The spectra are in accordance with the chemical composition as well as chemical states of the material. The signals at 147.18 and 152 eV in the core-level spectra of Pb in **Figure** 3b correspond to $4f_{7/2}$ and $4f_{5/2}$ levels respectively. In **Figure** 3c, the signal at 695.8 eV is a distinguishing feature of F 1s. The signals at 206 and 208 eV in **Figure** 3d are the characteristic features of Cl $2p_{3/2}$ and $2p_{1/2}$ respectively. The elemental ratios of Pb, F and Cl elements derived from XPS (1:0.45:0.55) which is close to the stoichiometric ratio of PbFCl.

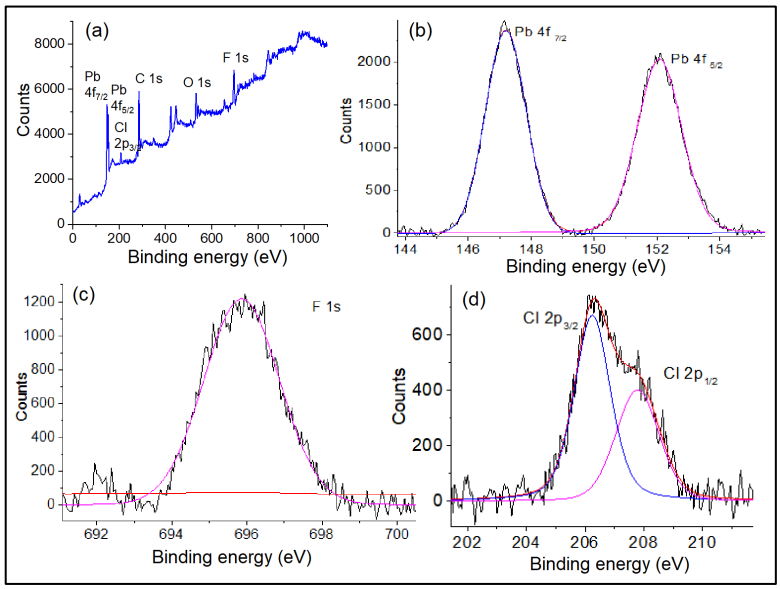

Figure 3: XPS spectra of PbFCl a) survey spectra (b, c, d) core-level spectra of Pb, F and Cl.

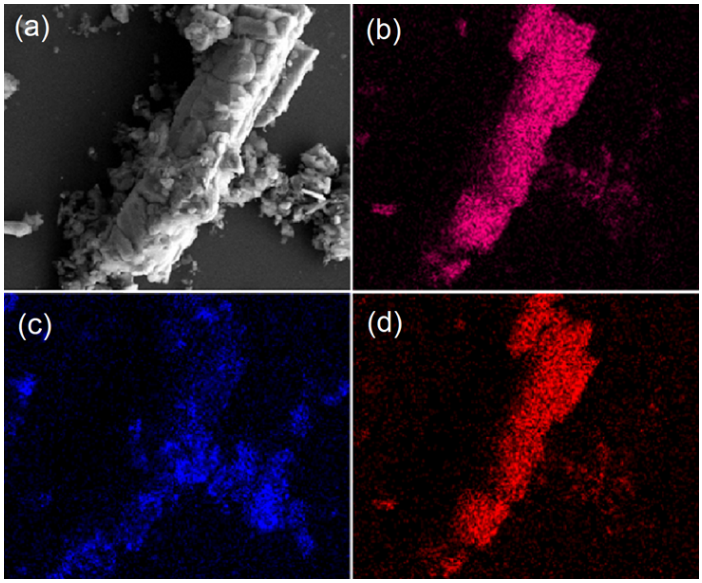

Figure 4. Elemental mapping of a) FESEM image b) Pb, c) F and d) Cl of PbFCl

Figure 4 shows elemental mapping of PbFCl obtained by using energy dispersive X-ray spectroscopy (EDS) which demonstrates the uniform distribution of Pb, F and Cl which is supported by XPS.

The Raman spectrum of PbFCl (**Figure** 5) which shows two strong bands at 131.7 and 163 cm^{-1} which can be attributed to E_g and A_{1g} modes respectively. We observe a weak band around 239 cm^{-1} which can be due to the E_g mode and the feeble band is at 103.2 cm^{-1} due to the A_{1g} mode.[17]

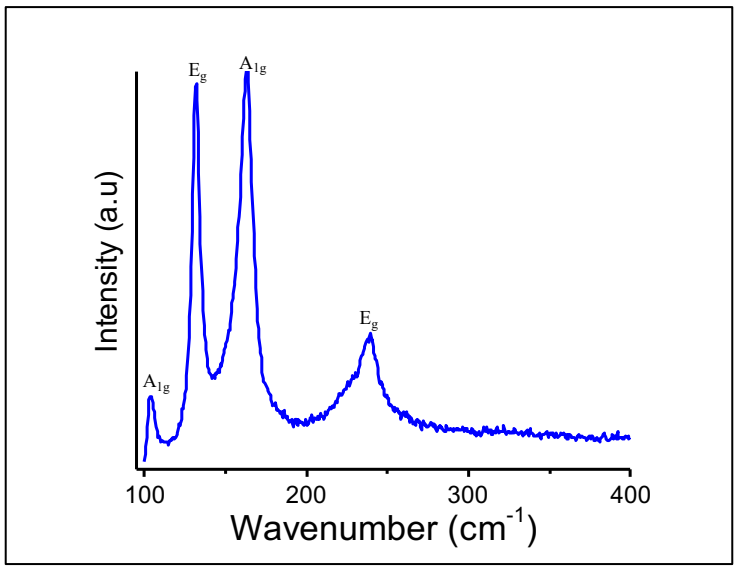

Figure 5: Raman spectrum of PbFCl.

Thermogravimetric analysis of PbFCl was carried out in the presence of oxygen (**Figure** 6). We observe, a sudden weight loss around 900 °C. The weight loss is more than 60% due to the conversion of PbFCl to PbO in the presence of oxygen. The formation of PbO was confirmed in XRD.

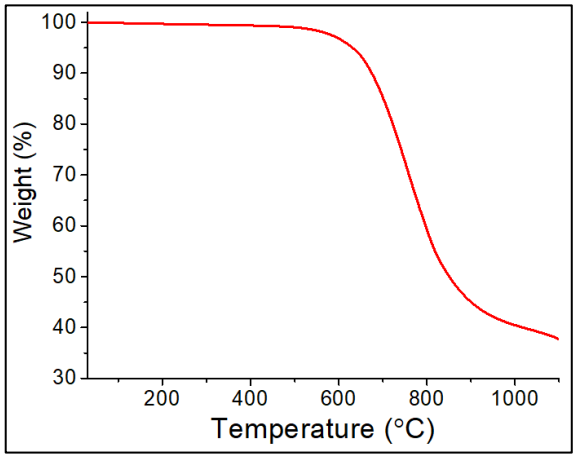

Figure 6: Thermogravimetric Analysis of PbFCl.

UV- Visible absorption spectra of bulk, as well as exfoliated PbFCl are given in **Figure** 7. A strong characteristic absorption band is occur at 267 nm of the PbFCl and the corresponding band gap calculated using Kulbeka-Munk equation is 4.64 eV. After exfoliation with water as a solvent, the absorption band is observed at 270 nm, a corresponding to a band gap of 4.58 eV. We note the absorption band of exfoliated PbFCl slightly red shifted compared to the bulk.

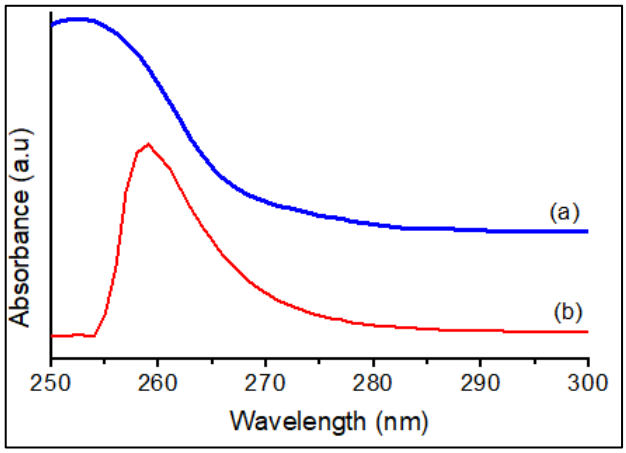

Figure 7: UV-Vis absorption spectra of a) PbFCl and b) PbFCl exfoliated in water.

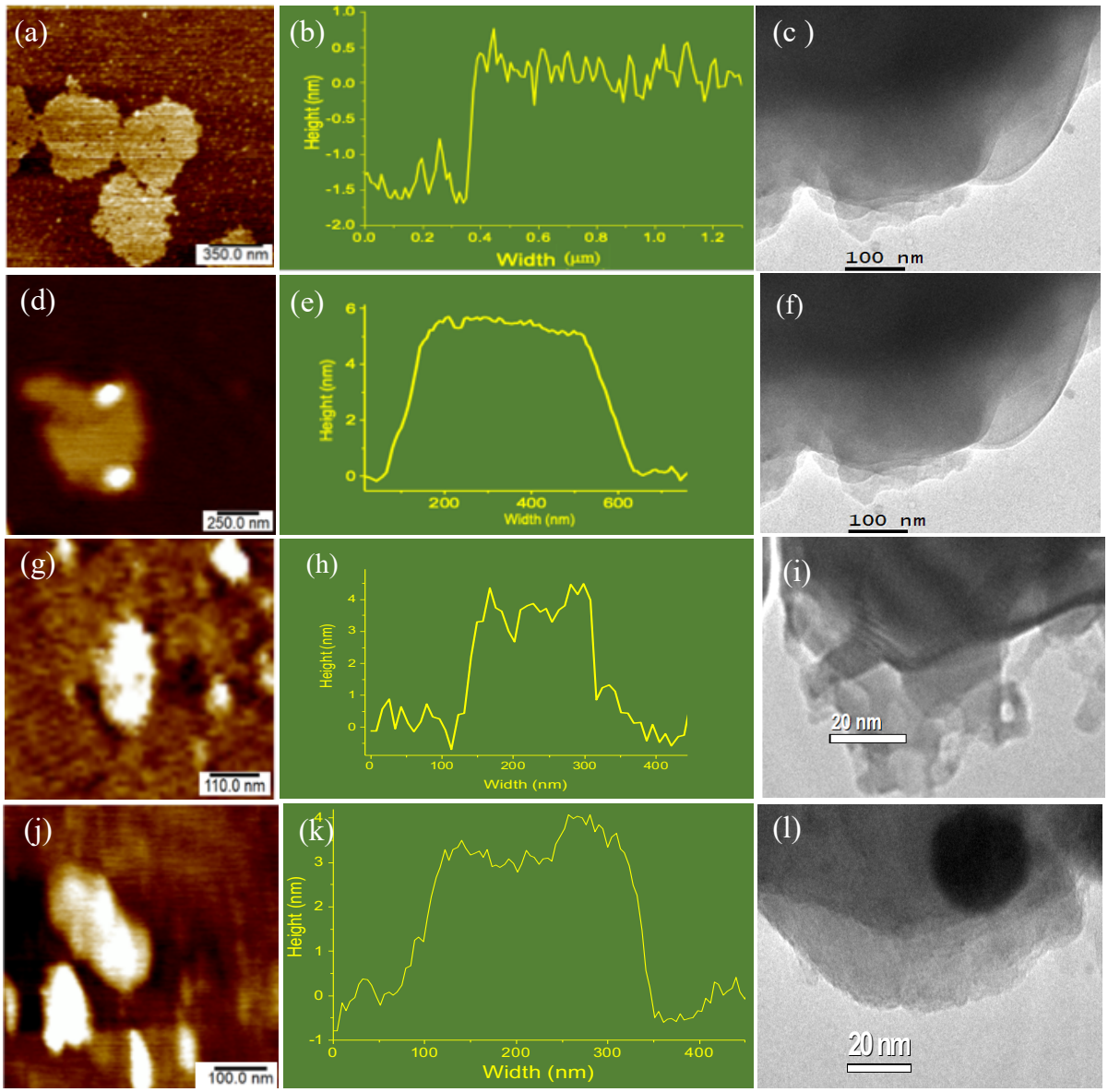

Figure 8. (a-c) Topographic AFM image, height profile and TEM image of e-PbFCl in water. (d-f) Topographic AFM image, height profile and TEM image of e-PbFCl in ethanol. (g-i) Topographic AFM image, height profile and TEM image of e-PbFCl in DMF. (j-l) Topographic AFM image, height profile and TEM image of e-PbFCl in NMP. (**Note**: e-PbFCl= exfoliated PbFCl).

Figure 8a shows topographic AFM of the exfoliated PbFCl in water, it demonstrates that PbFCl is exfoliated into monolayer with more than 90% yield and a thickness is ~1.2 nm and their lateral dimensions found to be few hundreds

of nm which is obtained from the height profile (**Figure** 8b). **Figure** 8c shows the TEM image of exfoliated PbFCl in water obtained by ultra-sonication which shows the characteristic feature of layered structure. PbFCl is also exfoliated in ethanol, DMF and NMP using the same procedure. **Figure** 8d shows a topographic AFM image and corresponding height profile (**Figure** 8e) of exfoliated PbFCl exfoliated in ethanol. We see that the thickness of the film is about 3-6 nm (3-5 layers of PbFCl with a yield of 20-30%) with a lateral dimension is few hundreds of nm. The corresponding TEM image is shown in **Figure** 8f. Exfoliation of PbFCl in DMF (**Figure** 8g) yields 20-30% of sheets of 5-8 layers with thickness 5-9 nm and width of ~500 nm. The height profile (**Figure** 8h) confirms this observation. The TEM image is shown in **Figure** 8i. **Figure** 8j shows a topographic AFM image of PbFCl exfoliated in NMP along with the height profile (**Figure** 8k) ~6 layers and a thickness of 7-9 nm. The sheets width is 400-700 nm. **Figure** 8l shows the TEM image of PbFCl-NMP in which layered structure seen at the edges.

Figure 9 show the FESEM images of bulk- and exfoliated PbFCl with different solvents. **Figure** 9a, displays flakes of bulk sample. PbFCl exfoliated with ethanol, DMF, NMP and water are shown in **Figure** 9b-e demonstrating flakes obtained after exfoliation.

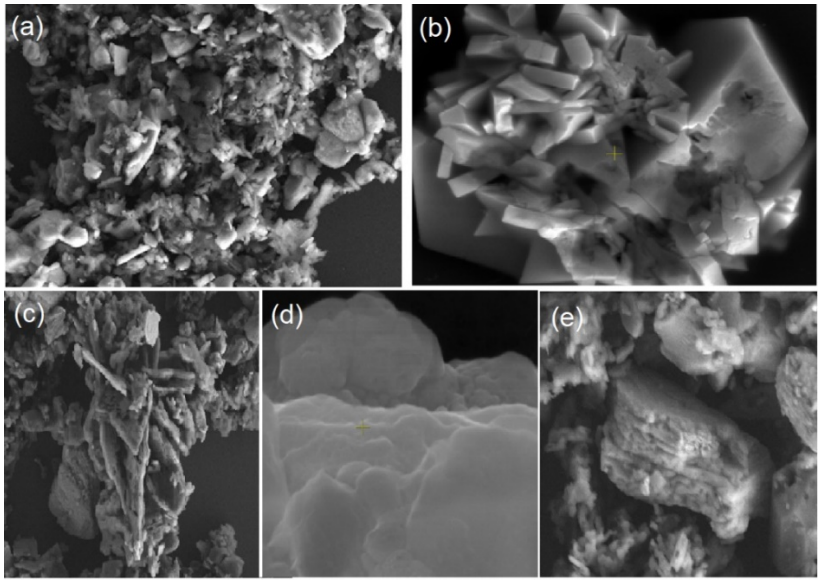

Figure 9: FESEM images of a) bulk-PbFCl, b-e) exfoliated PbFCl with water, ethanol, DMF and NMP

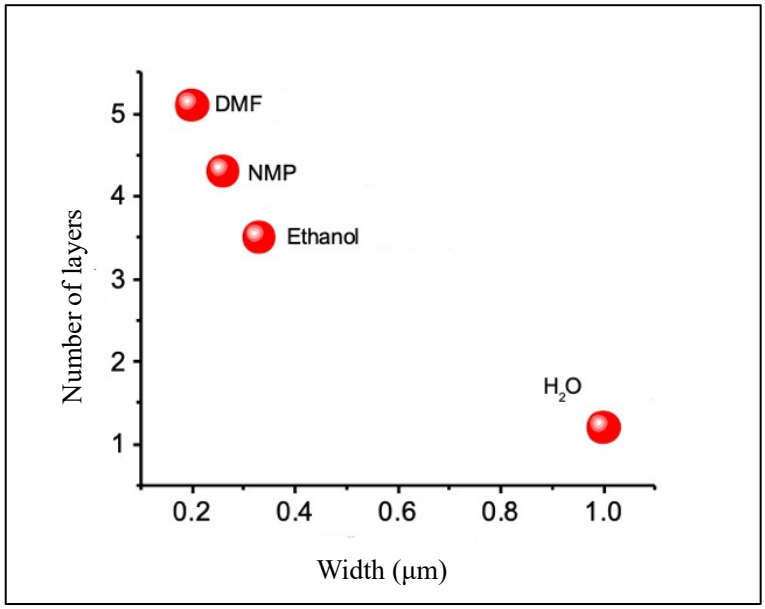

Figure 10. Graphical representation of exfoliation of PbFCl in different solvents

Figure 10 shows the pictorial graph of PbFCl exfoliation using different solvents, their thickness as well as percentage of exfoliation. Since Hansen Solubility Parameters (HSPs) of common organic solvents are already known, the HSP values (dispersibility, solubility, wettability, etc. as well as surface tension) of the probe solvents used in this study were obtained from HSP database which are listed in **Table** 1.[13] Exfoliation of PbFCl schematically presented in **Scheme** 1.

Solvent	Surface tension (mN/m) at 20 °C	δd/MPa$^{1/2}$	δp/MPa$^{1/2}$	δh/MPa$^{1/2}$	Total HSP	No. of exfoliated layers	% of exfoliation
H_2O	**72.8**	**15.6**	**16.0**	**42.3**	**47.8**	**1**	**> 90**
Ethanol	**22**	**15.8**	**8.8**	**19.4**	**26.5**	**3-5**	**20-30**
DMF	**37.1**	**17.4**	**13.7**	**11.3**	**24.9**	**5-8**	**20-30**
NMP	**41.2**	**18.0**	**12.3**	**24.9**	**23**	**4-8**	**< 20**

Table 1. Hansen Solubility parameters of different solvents used for exfoliation of PbFCl.

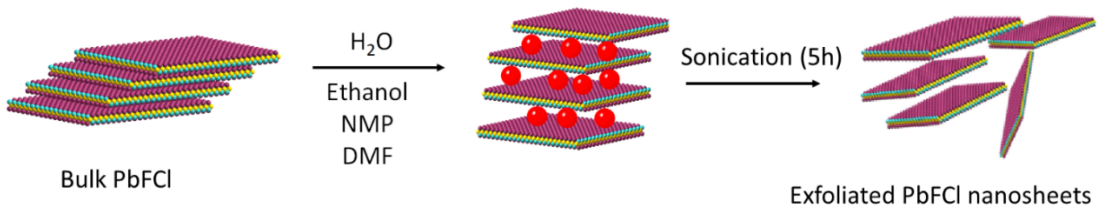

Scheme 1. Schematic representation of exfoliation of PbFCl with various solvents.

The effect of intercalation of different compounds in PbFCl sheets has been studied. It was found that small molecules such as ethyl methyl ether, hexane, can easily intercalate into the van der Waals gap without structure deformation. However, intercalation with the surfactant, cetyltrimethylammonium bromide (CTAB) and 1,2-methyl-ethyl-imidazolium tetrafluoroborate **Figure** 11 (i) cause a large expansion of van der Waals space (**Scheme** 2).

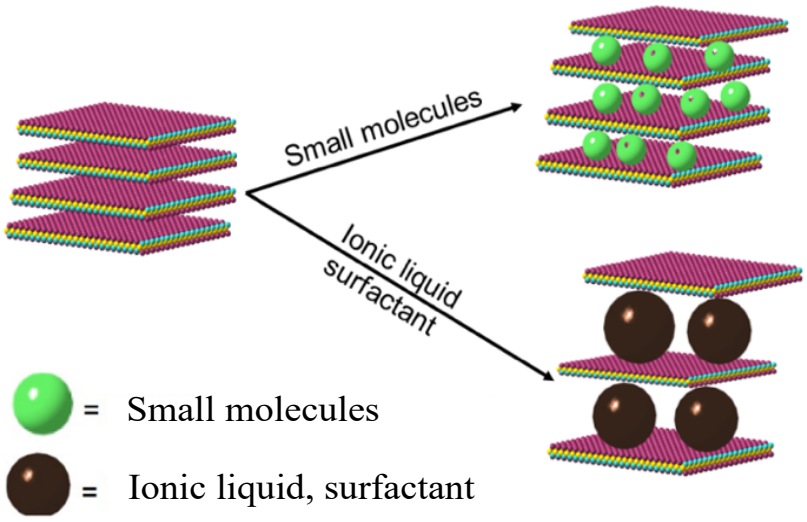

Scheme 2. Schematic diagram of intercalation of PbFCl with organic compounds

Figure 11(ii) shows the shift of (001) plane of XRD after intercalation of various solvents and corresponding FTIR is shown in **Figure** 12. Variation of the interlayer spaces of PbFCl with different organic solvents is evaluated from d-space of XRD and depicted in **Table** 2.

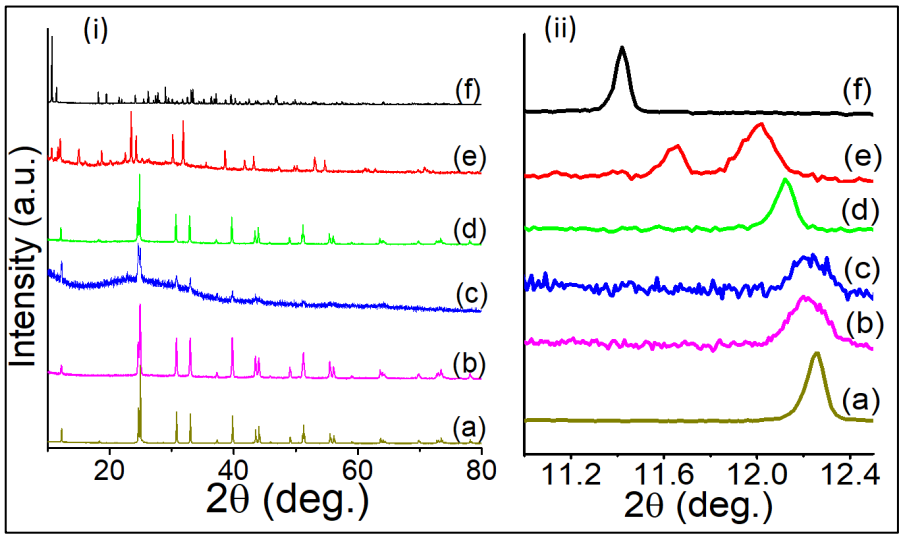

Figure 11: (i) XRD spectra of PbFCl functionalization with various organic solvents (b) ethyl methyl ether, (c) hexane, (d) pentadecane, (e) CTAB and (f) 1,2-methyl-ethyl-imidazolium tetrafluoroborate. (Note: (a) bulk PbFCl) and (ii) Small angle shift of (001) plane with respect to (a).

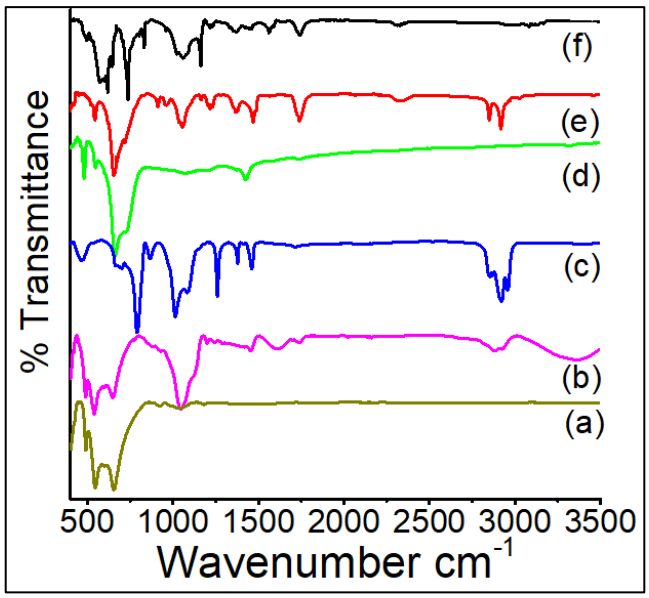

Figure 12: FTIR spectra of PbFCl functionalization with various organic solvents (b) ethyl methyl ether, (c) hexane, (d) pentadecane, (e) CTAB and (f) 1,2-methyl-ethyl-imidazolium tetrafluoroborate. (Note: (a) bulk PbFCl).

Sl.No.	Name of the solvent	PbFCl Interlayer space (Å)	Interlayer space after intercalation (Å)	Interlayer space difference (Å)
2	Ionic liquid (1-ethyl-3-methyl imidazolium tetrafluoroborate)	0.419	0.949	0.53
3	Surfactant (CTAB)	0.419	0.569	0.15
4	Pentadecane	0.419	0.499	0.08
5	Methyl-ethyl ether	0.419	0.459	0.04
6	Hexane	0.419	0.449	0.03

Table 2: Interlayer spaces of PbFCl after intercalation.

Conclusions

In conclusion, we have synthesized 2D-layered PbFCl by solid state synthesis. The liquid exfoliation has been carried out of the as synthesized PbFCl in various solvents namely water, ethanol, NMP, DMF. We have found that PbFCl is exfoliated in water into monolayer with more than 90% yield. We observed no significant change in the band-gap of bulk and exfoliated PbFCl. Intercalation was carried out with molecules of various size like ethyl methyl ether, hexane, pentadecane, ionic liquids and surfactants. We observed that small size non-polar molecules like ethyl methyl ether and hexane were intercalated in the van der Waals gap of the layers. Whereas molecules with high polarity like surfactants and ionic liquids were not intercalated and led to the structural deformation of PbFCl.

References

[1] A. K. Geim, K. S. Novoselov, *Nature Materials* **2007,** *6*, 183.

[2] C. N. R. Rao, A. K. Sood, K. S. Subrahmanyam, A. Govindaraj, *Angewandte Chemie International Edition* **2009**, *48*, 7752.

[3] C. N. R. Rao, H. S. S. Ramakrishna Matte, U. Maitra, *Angewandte Chemie International Edition* **2013**, *52*, 13162.

[4] C. N. R. Rao, U. V. Waghmare, *2D Inorganic Materials beyond Graphene*; World Scientific; **2016**.

[5] M. Chhowalla, D. Jena, H. Zhang, *Nature Reviews Materials* **2016**, *1*.

[6] B. Radisavljevic, A. Radenovic, J. Brivio, V. Giacometti, A. Kis, *Nature Nanotechnology* **2011**, *6*, 147.

[7] S. Z. Butler, S. M. Hollen, L. Cao, Y. Cui, J. A. Gupta, H. R. Gutiérrez, T. F. Heinz, S. S. Hong, J. Huang, A. F. Ismach, E. Johnston-Halperin, M. Kuno, V. V. Plashnitsa, R. D. Robinson, R. S. Ruoff, S. Salahuddin, J. Shan, L. Shi, M. G. Spencer, M. Terrones, W. Windl, J. E. Goldberger, *ACS Nano* **2013**, *7*, 2898.

[8] M. K. Jana, C. N. R. Rao, *Philosophical Transactions of the Royal Society A: Mathematical, Physical and Engineering Sciences* **2016**, *374*, 20150318.

[9] N. Mounet, M. Gibertini, P. Schwaller, D. Campi, A. Merkys, A. Marrazzo, T. Sohier, I. E. Castelli, A. Cepellotti, G. Pizzi, N. Marzari, *Nature Nanotechnology* **2018**, *13*, 246.

[10] A. H. Reshak, Z. Charifi, H. Baaziz, *The European Physical Journal B* **2007**, *60*, 463.

[11] F. E. haj Hassan, H. Akbarzadeh, S. J. Hashemifar, A. Mokhtari, *Journal of Physics and Chemistry of Solids* **2004**, *65*, 1871.

[12] H. Hagemann, A. Rief, F. Kubel, J. L. M. van Mechelen, F. Tran, P. Blaha, *Journal of Physics: Condensed Matter* **2007**, *19*, 036214.

[13] C. Hansen, T. Poulsen, *Hansen Solubility Parameters* **2007**, 269.

[14] https://www.hansen-solubility.com/, Hansen Solubility Parameters.

[15] Charles M. Hansen, *Hansen Solubility Parameters: A User's Handbook*; 2nd ed.; CRC Press, **2012**.

[16] H. E. Swanson, E. Tatge, *Journal of Research of the National Bureau of Standards* **1951**, *46*, 318.

[17] A. Rulmont, *Spectrochimica Acta Part A: Molecular Spectroscopy* **1974**, *30*, 161.

CHAPTER 2

Covalently-linked 2H-MoS_2 and $MoSe_2$ with other 2D layered materials and stable the 1T-forms by hydrothermal and solvothermal methods, showing remarkable photochemical HER activity*

SUMMARY

Transition metal dichalcogenides (TMDC) are promising materials as photocatalysts. In this study we have focused on MoS_2 and $MoSe_2$ as they have low activity in stable 2H-form but after the cross-linking with the other 2D layered materials like borocarbonitride etc. their activity improves many fold. Nanocomposites like, $MoSe_2$–$MoSe_2$ and $MoSe_2$–BCN show high photocatalytic activity even in the 2H form. This study shows the important role played by covalent cross-linking of layered compounds. Photocatalytic activity of covalently cross-linked layer of 2H-$MoSe_2$ is higher than that of 2H-MoS_2. Unlike the 2H forms, the metallic 1T forms of MoS_2 and $MoSe_2$ prepared by Li-intercalation followed by exfoliation, exhibit high photocatalytic hydrogen evolution reaction (HER) activity. The materials prepared by Li- intercalation are however, unstable. The 1T forms of MoS_2 and $MoSe_2$ prepared by solvothermal or hydrothermal methods are quite stable and exhibit good photochemical activity for HER. The 1T forms are generally superior to the covalently linked 2H forms. The present study shows how MoS_2 and $MoSe_2$ in both 2H and 1T forms can be exploited for photochemical HER activity by appropriate chemical manipulation.

* A paper related to this work has appeared in *J. Chem. Sci. (2018)*

3.1 Introduction

In recent decades excessive use of non-renewable energy sources like fossil fuels have caused increase in environment pollution particularly air pollution and global warming.[1–3] According to recent reports, much of air pollution is generated by the burning of fossil fuels such as petrol, diesel, coal, oil, natural gas etc. for transportation, electricity production, heating and industry. Worldwide in 2014 , 81% of total primary energy supply.[4] Due to the limited supply of the non-renewable energy sources for the future generation to sustain, we need to shift towards a renewable, environment friendly, high efficiency fuels. Hydrogen is one of the good alternatives[2] for the purpose but the process is to develop hydrogen as an alternative is still in nascent stages. There are several ways to generate hydrogen,[5] but one of the means is from water splitting wherein hydrogen is obtained from water by using catalysts[6–9] MoS_2 has gained considerable importance in this context. Unlike the semiconducting 2H form of MoS_2, the metallic 1T form exhibits outstanding performance in photochemical hydrogen generation, the 1T form of $MoSe_2$ being even better. The 1T forms are obtained in the form of nanosheets by intercalating Li in the stable 2H-MoS_2 or $MoSe_2$ followed by exfoliation in water. 1T-MoS_2 and $MoSe_2$ prepared in this way are unstable, and transform to the stable 2H forms on keeping.[10] Stable 1T-MoS_2 and $MoSe_2$ can be prepared by hydrothermal and solvothermal methods.[11] An interesting discovery in recent months is the advantage of coupling sheets of stable 2H-MoS_2 with other layered materials to enhance the catalytic activity for hydrogen evolution.[12–15] One of the important members of this class of materials obtained by cross-linking two layered structures is that obtained by cross-linking MoS_2 with a carbon-rich borocarbonitride, BC_7N.[14] Note that MoS_2 here is in the 2H form. Since it is known that $MoSe_2$ may have more desirable characteristics for use as a catalyst for hydrogen generation,[10] we have considered it important to investigate HER activity of $MoSe_2$ cross-linked with

the other 2D materials. It is indeed reported that 1T-$MoSe_2$ sheets are superior to sheets of 1T-MoS_2 as catalysts in the photochemical generation of hydrogen.[10] In view of this background, we have investigated nanosheets of 2H-$MoSe_2$ cross-linked with C_3N_4 and the carbon-rich borocarbonitride, BC_7N. We have used the simpler term BCN, to designate borocarbonitride. We have prepared the BCN–$MoSe_2$ composites where BN domains of borocarbonitride are cross-linked to $MoSe_2$ nanosheets (BN/BCN–$MoSe_2$) and also composites where the graphene domains of borocarbonitride are cross-linked with $MoSe_2$ sheets (G/BCN–$MoSe_2$). In addition, we have investigated assemblies of $MoSe_2$ layers in order to compare the performance of these materials with those of single layer of $MoSe_2$ and cross-linked layers of MoS_2.

Besides investigating the photochemical generation of hydrogen with semiconducting 2H-$MoSe_2$,[16,17] covalently bonded with sheets of C_3N_4,[18,19] BC_7N [20,21] and with itself, we have examined photochemical hydrogen generation by the metallic 1T forms of MoS_2 and $MoSe_2$ prepared by hydrothermal and solvothermal methods. It is to be noted that the 1T forms of Mo dichalcogenides[22,23] prepared solvothermally or hydrothermally would not be expected to be identical to the 1T forms prepared by Li-intercalation and exfoliation, differing in surface properties.

3.2 Experimental

Synthesis of cross-linked $MoSe_2$ nanosheets

$MoSe_2$ layers cross-linked with the layers of other 2D materials were generally prepared as follows. Nanosheets of 1T-$MoSe_2$ were generated by Li- intercalation of 2H-$MoSe_2$, followed by exfoliation in deionized water.[10] 1T-$MoSe_2$ layers were reacted with a 10-fold excess of 2-bromoacetic acid to obtain the surface carboxyl groups by forming the C–Se bond ($MoSe_2$–CH_2 COOH). The surface

carboxyl groups of $MoSe_2$ were utilized to link with nanosheets of other 2D materials. Similarly, 1T-$MoSe_2$ layers were reacted with a 12-fold excess of the 4-iodoaniline to obtain the surface amine groups by forming the C–Se bonds[24] ($MoSe_2$–$C_6H_4NH_2$). The surface amine groups of $MoSe_2$ were utilized for linking with other sheets.

Assemblies of $MoSe_2$ could be prepared by the reaction of 1T-$MoSe_2$ with diazonium salt of 4-iodoaniline to obtain iodobenzene functionalized $MoSe_2$ ($MoSe_2$–C_6H_4I), followed by addition of 1T-$MoSe_2$ to form $MoSe_2$ assemblies by forming the C–Se bonds[24] ($MoSe_2$ –C_6 H_4 –$MoSe_2$) (**Scheme** 1).

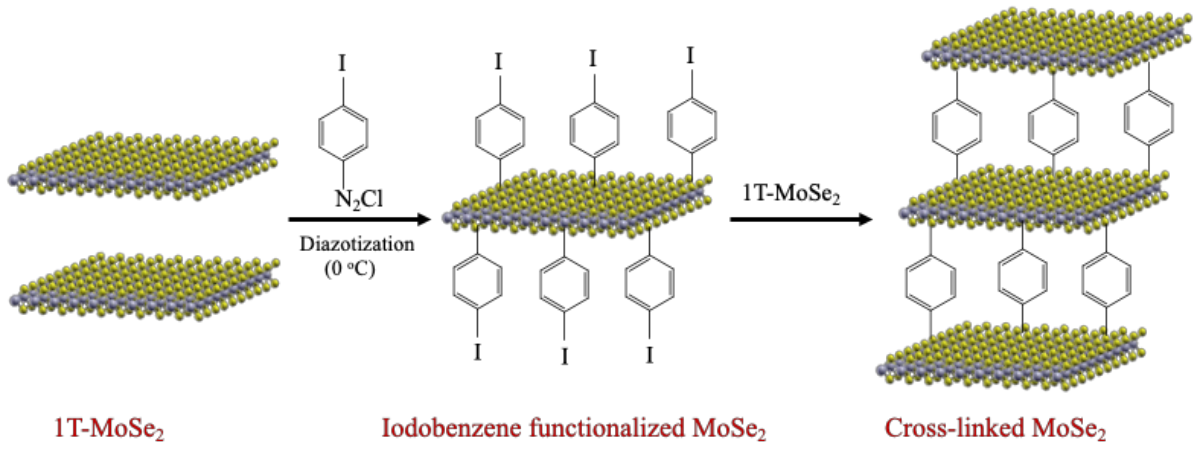

Scheme 1: Synthesis of cross-linked $MoSe_2$-$MoSe_2$ nanosheets

To obtain cross-linked $MoSe_2$–C_3N_4, $MoSe_2$–CH_2COOH (30mg) and C_3N_4 (30 mg) were dispersed in dry DMF in nitrogen atmosphere. To the above dispersion, equal amounts of 1- hydroxybenzotriazole (HOBt, 30mg) and N-(3-(dimethylamino)propyl)-N′ -ethylcarbodiimidehydrochloride (EDC·HCl, 30 mg) were added along with N,N-diisopropyl ethylamine (DIPEA, 500 µL) and stirred at room temperature for 48 hours in an inert atmosphere which was maintained during the reaction. The solid product was collected by filtering, then washed with DMF and dried at 60 °C under vacuum (**Scheme** 2).

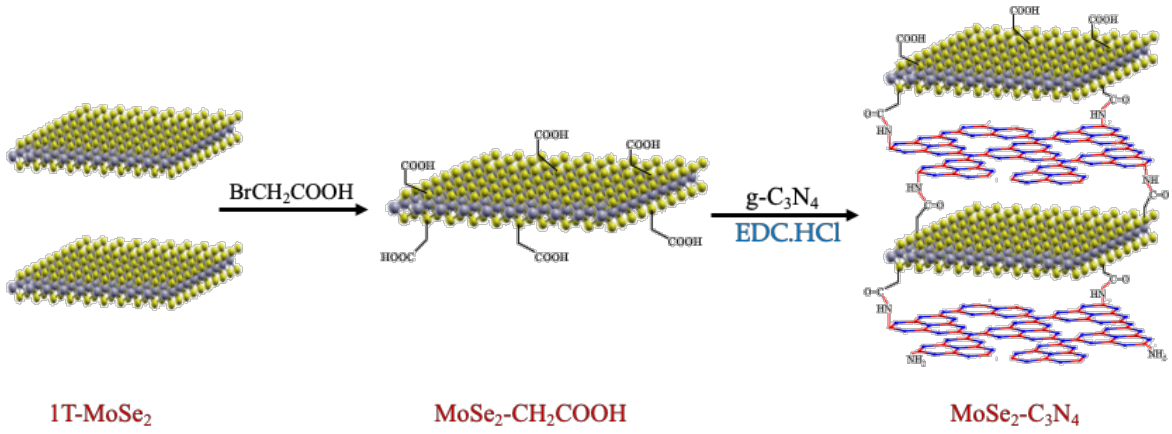

Scheme 2 : Synthesis of cross linked chain of $MoSe_2$–C_3N_4

Borocarbonitride nanosheets were synthesized by using an already reported method.[20,25] Starting with activated charcoal (500 mg), urea (2.4 g) and boric acid (60 mg) were heated in a furnace at 900 °C in nitrogen atmosphere for 10 hours. The black product was treated with NH_3 at 900 °C for 5 hours. Hence, these are the two possible ways of linking $MoSe_2$ nanosheets of other 2D materials: by linking to BN domains in BC_7N (BN/BCN–$MoSe_2$) and by linking to graphene (G) domains in BC_7N (G/BCN–$MoSe_2$) as shown in **Scheme** 3.

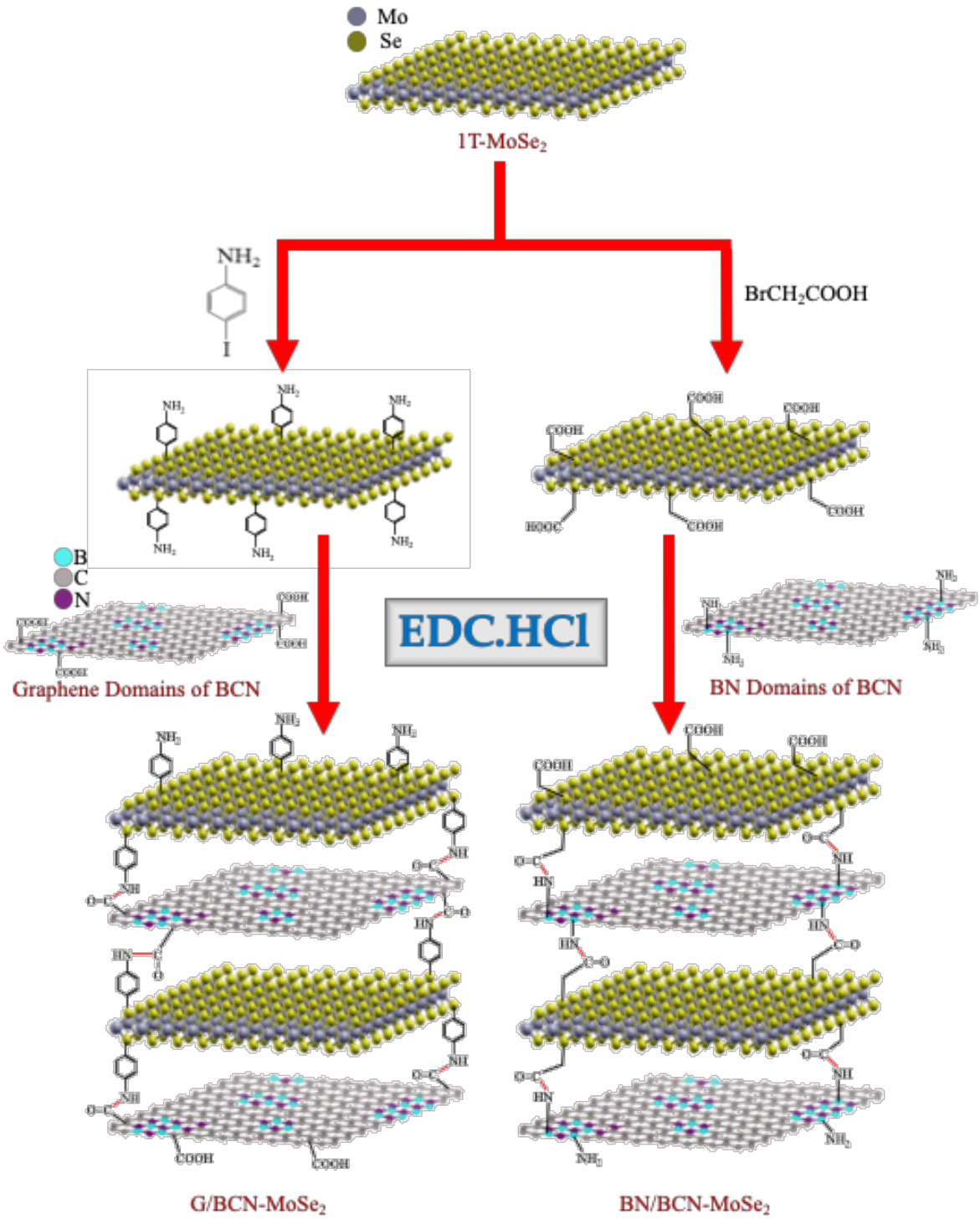

Scheme 3: Synthesis of covalently cross-linked G/BCN–$MoSe_2$ and BN/BCN–$MoSe_2$ nanocomposites (EDC = 1-ethyl-3-(3 dimethylaminopropyl)carbodiimide).

Solvothermal synthesis of 1T-MoS_2 and 1T-$MoSe_2$

1mmol of $MoCl_5$ (from Alfa Aesar, 99% Purity) and 10.1 mmol of thioacetamide (CH_3CSNH_2) (Loba Chemie, 99% Purity) were dissolved in 30 mL of DMF (SD Fine chemicals, 99% Purity). The solution was stirred for 30 minutes and then transferred to a 25 mL Teflon-lined autoclave. The autoclave was heated at 200 °C for 30 hours.[26] Similarly, 1T-MoSe2 was prepared in DMF taking 0.1 mmol of $MoCl_5$, and 3 mmol of Selenourea (Alfa Aesar, 99% Purity) dissolved in 20 mL of DMF. The solution was stirred for 30 minutes and transferred to a 25 mL Teflon-lined autoclave. The autoclave was heated up to 200 °C for 48 hours. Then autoclave was allowed to cool to room temperature, and the product was washed several times with water and ethanol and dried at 60 °C under vacuum.

Hydrothermal synthesis of 1T-MoS_2 and 1T-$MoSe_2$

1T-MoS_2 was synthesized hydrothermally by dissolving 1mmol of ($NaMoO_4 \cdot 2H_2O$, Merck 99%) and 3 mmol of thiourea ($CS(NH_2)_2$, SD Fine chemicals, 99%) in a solution of water and propionic acid (2:1). The solution was magnetically stirred for 30 minutes then transferred into 25 mL Teflon-lined autoclave, heated at 200 °C for 4 hours.[27] Selenourea was used as a precursor to synthesize 1T-$MoSe_2$. 1T-$MoSe_2$ was synthesized by dissolving 1 mmol of ($NaMoO_4 \cdot 2H_2O$, Merck 99%) and 3 mmol of Selenourea (Alfa Aesar chemicals, 99%) in a solution of water and propionic acid (2:1). The solution was stirred for 30 minutes and then transferred into a 25 mL Teflon- lined autoclave, heated at 200 °C for 4 hours. The autoclave was allowed to cool to room temperature and the product washed several times with water and alcohol and allowed to dry at 60 °C in a vacuum oven for 24 hours.

Characterization

Fourier-transform infrared (FTIR) spectra were recorded with Bruker IFS 66v/S spectrometer. Scanning electron microscope (SEM) images were obtained with FEI Nova Nano SEM 600 microscope. Powder X-ray diffraction (PXRD) data were collected with Bruker diffractometer (Cu Kα (λ = 1.5406 Å) X-ray source). Raman spectra were collected with Jobin Yvon LabRam HR spectrometer using Ar-laser (λ = 514.5 nm). Transmission electron microscope (TEM) images were collected by FEI Tecnai microscope, operating at 200 kV accelerating voltage. High-resolution TEM (HRTEM) was obtained with FEI Titan aberration-corrected electron microscopy. X-ray photoelectron spectra (XPS) was recorded with an Omicron spectrometer using Al Kα as the X-ray source (1486.6 eV). Nitrogen adsorption-desorption isotherms (77 K) were obtained using a QUANTACHROME QUADRASORB-SI analyser. The samples were first heated in vacuum at 80 °C for approximately 24 hours and then the adsorbate charged into the sample tube. The pressure change was monitored to observed a decrease in pressure at equilibrium, using which the degree of adsorption was determined.

Photocatalytic hydrogen evolution reaction

Scheme 4 shows the principle of the method we have used. 2.5 mg of the catalyst was dispersed in an aqueous solution of triethanolamine (15% v/v, 48 mL) by sonication in a cylindrical glass vessel. Eosin Y (EY) (14 μmol) was added as a sensitizer. This mixture was illuminated with a halogen lamp (100 W) under constant stirring. The evolved gas was manually collected from the headspace and analysed with a gas chromatograph equipped with a thermal conductivity detector (PerkinElmer ARNL 580C).

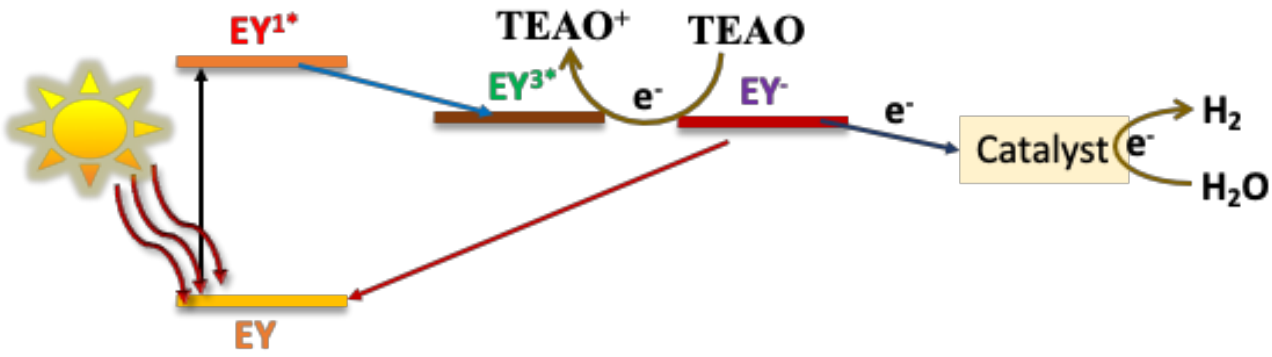

Scheme 4: Schematic diagram of electronic states of EY and plausible mechanism of hydrogen evolution reaction.

The **Scheme** 4 represents a singlet ground-state as EY, excited singlet state EY^{1*}, and low lying triplet state EY^{3*}. The highly reducing negatively charged state (EY^{-}) forms in the presence of triethanolamine (TEOA). The electron from the reducing species is transferred to the catalyst for hydrogen evolution reaction.

3.3 Results and discussion

$MoSe_2$ cross-linked to C_3N_4 and BC_7N and as well as the assembly of $MoSe_2$ were characterized by FTIR and Raman spectroscopy, XRD and other techniques.

The FTIR spectrum of $MoSe_2$–CH_2COOH shows strong bands at 1758 and 3210 cm^{-1} which correspond to C=O and –OH stretching vibrations of carboxylic groups beside with a C-Se stretching band at 736 cm^{-1} arising from covalent functionalization. BC_7N displays a strong band at 1591 cm^{-1} and a weak band around 1723 cm^{-1} arising from C=C and C=O stretching vibrations respectively along with a broad band in the 3065–3485 cm^{-1} region corresponding to the residual amine and hydroxyl groups. The broad band around 950–1250 cm^{-1} is due to C–O stretching and O–H bending vibrations. The C=O stretching band in G/BCN–$MoSe_2$ composite at 1638 cm^{-1} along with other characteristic bands

from amino benzene moieties suggests the formation of amide linkages between carboxylic groups of graphene domains of BC_7N and amine functionalized $MoSe_2$. Similarly, BN/BCN $MoSe_2$ nanocomposite shows a carbonyl stretching band at 1676 cm^{-1}, confirming cross-linking of the BC_7N and $MoSe_2$ layers by the amide bond (**Figure** 1a and 1b).[28]

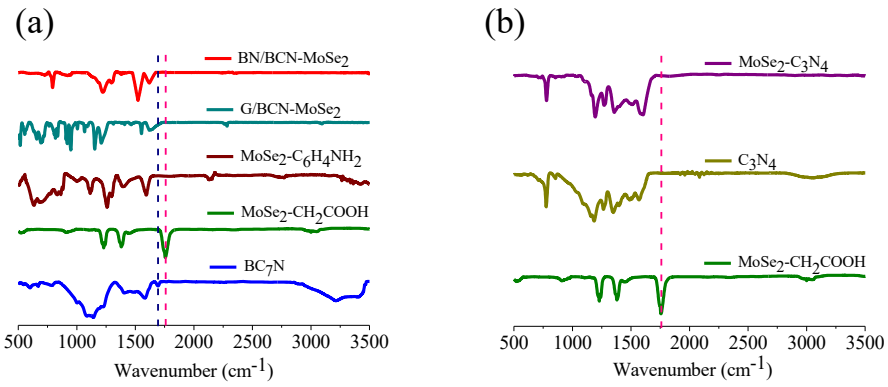

Figure 1: (a, b) FTIR spectrum of $MoSe_2$ and its nanocomposites

Raman spectroscopy plays a crucial role in determining the stable form of $MoSe_2$ structure in the cross-linked nanocomposite. Raman spectra of BCN–$MoSe_2$ nanocomposite are presented in **Figure** 2. The spectra of the G/BCN–$MoSe_2$ and BN/BCN-$MoSe_2$ nanocomposites show characteristic D and G bands of BC_7N at 1349 and 1606 cm^{-1}, respectively, along with the A_{1g} and E^1_{2g} bands of $MoSe_2$ at 244 and 291 cm^{-1}, respectively.[29] 2H form of $MoSe_2$ is observed in nanocomposites.

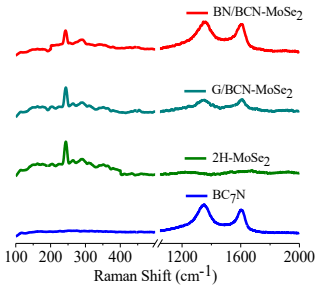

Figure 2: Raman spectra of $MoSe_2$ and its nanocomposites.

The formation of covalent cross-linked assemblies was also investigated using PXRD patterns of BN/BCN-$MoSe_2$, G/BCN–$MoSe_2$ and $MoSe_2$ –C_3N_4 nanocomposites which showed the appearance of new reflections at 2θ =13.19°(d=0.67 nm), 12.76°(d=0.69 nm) and 13.09°(d=0.68 nm) corresponding to the interlayer spacing between BC_7N–$MoSe_2$ and $MoSe_2$–C_3N_4 nanocomposites.

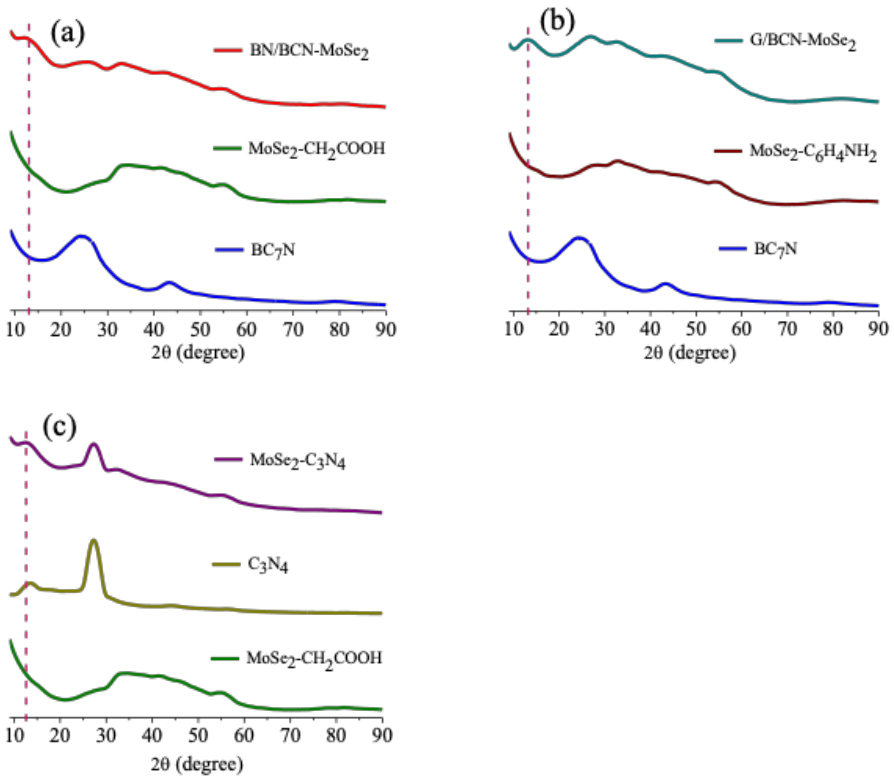

Figure 3: PXRD pattern of BCN, $MoSe_2$ and their nanocomposites.

SEM and TEM images of the $MoSe_2$ assemblies, G/BC_7N–$MoSe_2$ and BN/BC_7N–$MoSe_2$ showed evidence for layer-by-layer assembly of sheet structure upon cross-linking of the constituent $MoSe_2$ and BC_7N layers.

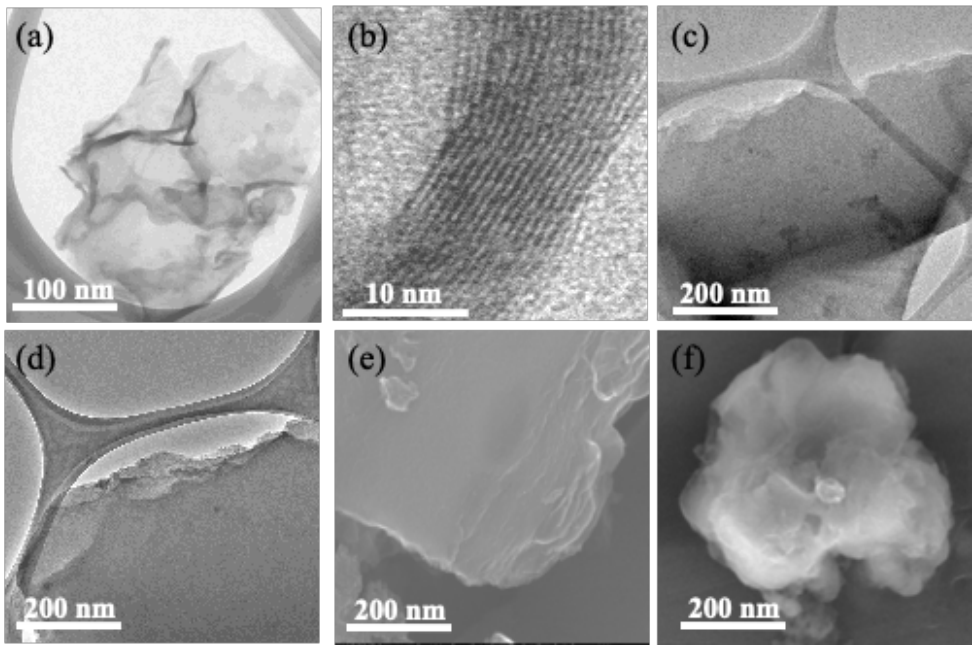

Figure 4: (a, b) HRTEM image of $MoSe_2$ and crosslinked $MoSe_2$- $MoSe_2$, (c, d) TEM image of BCN with cross-linking of $MoSe_2$, BN/BCN- $MoSe_2$ and G/BCN- $MoSe_2$, (e, f) SEM image of crosslinked $MoSe_2$- $MoSe_2$ and $MoSe_2$-C_3N_4.

The surface areas of nanocomposites were also calculated from BET nitrogen adsorption-desorption isotherms (at 77 K) for BCN–$MoSe_2$, $MoSe_2$–$MoSe_2$, $MoSe_2$–C_3N_4 nanocomposites and $MoSe_2$ done are 580, 312, 280 and 78 m^2/g respectively. Type-I characteristics in the low-pressure region along with a type-II hysteresis loop in the high-pressure region, as per the IUPAC nomenclature.[30]

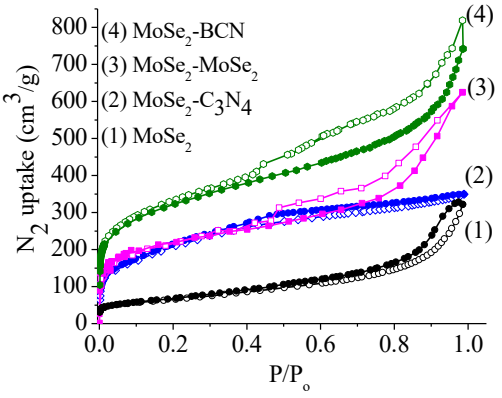

Figure 5: Nitrogen sorption profiles of (1) $MoSe_2$, (2) $MoSe_2$-C_3N_4, (3) $MoSe_2$-$MoSe_2$ and (4) $MoSe_2$-BCN.

To find out the nature of bonding the XPS were carried out by drop-casting the well dispersed sample on silicon substrate. **Figure** 6 shows the spectra of BC_7N with the core level spectrum of C, B, N respectively. The C 1s spectra can be fitted into four peaks at 283.7, 284.4, 285.6 and 286.8 eV due to C-B bonds, sp^2 carbons, C-N bonds and surface carbonyl respectively. The B 1s can be fitted into three peaks centred at 190.9, 192.3 and 194.1 eV due to B-C, B-N, B-O bonds respectively. The nitrogen spectra can be fitted into three peaks 397.9, 399.7, 399.8 eV which corresponds to the B-N bonds, pyrrolic group and graphitic group respectively.

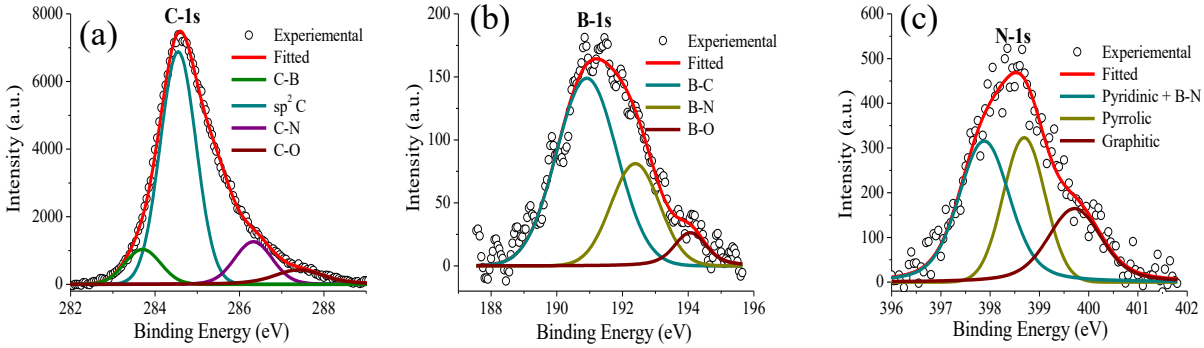

Figure 6: (a), (b) and (c) showing the core level XPS of C, B and N respectively.

To prove the cross-linking of $MoSe_2$-$MoSe_2$ XPS carried out of Iodobenzene functionalised $MoSe_2$ and Cross-linked $MoSe_2$, the peak of $I3d_{5/2}$ and $I3d_{3/2}$ is negligible in case of cross-linked $MoSe_2$.

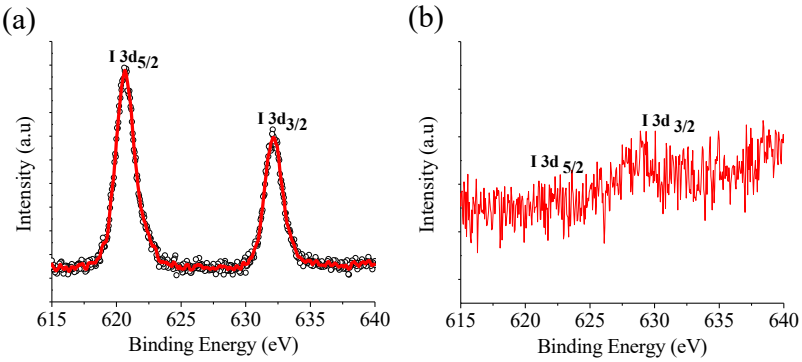

Figure 7: XPS of (a) Iodobenzene functionalized $MoSe_2$ and (b) Cross-linked $MoSe_2$.

Study of the photochemical hydrogen evolution have done in the presence of Eosin Y(as a sensitizer) in aqueous solution triethanolamine (TEOA, as a sacrificial agent). The mechanism of hydrogen evolution with reaction Eosin Y and the triethanolamine is well-studied in the literature(**Scheme** 4).[10,31] Comparison of the results of photochemical hydrogen yields of nanocomposites of MoS_2 and $MoSe_2$. Pristine MoS_2 and $MoSe_2$ show a similar activity of 1663 and 1680 $\mu molg^{-1}h^{-1}$, respectively.[14]. Pristine BC_7N and pristine C_3N_4 show very low activity 165 and 113 $\mu molg^{-1}h^{-1}$ respectively, (**Figure** 8).The self-assembly of $MoSe_2$ however, shows high activity of 8294 $\mu molg^{-1}h^{-1}$. This is much higher than that of MoS_2 assemblies(1750 $\mu molg^{-1}h^{-1}$) synthesized by the same method.[12] $MoSe_2$–C_3N_4 nanocomposite exhibits a somewhat lower activity 2624 $\mu molg^{-1}h^{-1}$ compared to MoS_2–C_3N_4. This is unlike BC_7N–$MoSe_2$ which exhibits a high activity 10384 or 12584 $\mu molg^{-1}h^{-1}$ compared to BC_7N–MoS_2 6965 $\mu molg^{-1}h^{-1}$. (**Figure** 8).

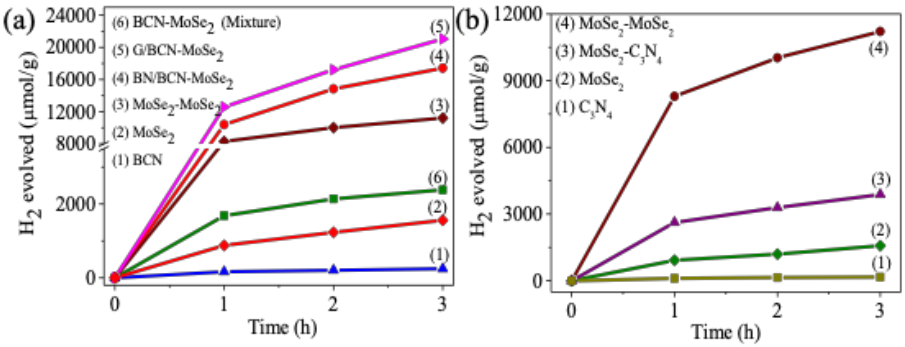

Figure 8: (a, b) Comparison of the H_2 evolution activity of $MoSe_2$ and its nanocomposites.

It is interesting to note that the photochemical activity and surface area vary in the same fashion. The increased HER activity in the cross- linked composites increases with the surface area as cross-linking opens up pores and slits where edges can act as HER sites. Moreover, cross-linking increases the planarity of the layer with increased overlap between the cross-linked layers, facilitating charge transfer across the network.[13] Moreover, HER with the physical mixture of BCN

and $MoSe_2$ shows very small activity (878 $\mu molg^{-1}h^{-1}$) which is much lower compared to the cross-linked material. This observation suggests that cross-linking has a role in enhancing the HER activity (**Table** 1). [13–15]

Materials	**Surface area** **(m^2/g)**	**Activity** **[$\mu mol\ g^{-1}\ h^{-1}$]**
2H-$MoSe_2$	78	1680
BCN	810	165
C_3N_4	29	113
$MoSe_2$- $MoSe_2$	312	8294
$MoSe_2$- C_3N_4	280	2624
BN/BCN- $MoSe_2$	580	10384
G/BCN- $MoSe_2$	576	12584
BCN- $MoSe_2$ **Physical Mixture**	-	878

Table 1: Photochemical HER activity of nanocomposites of 2H-$MoSe_2$ cross-linked with other 2D layers.

The activity of assemblies of BCN–$MoSe_2$ nanocomposite is especially noteworthy. We can compare the performance of the $MoSe_2$ nanocomposites with

those of MoS_2. The performance of $MoSe_2$ nanocomposites is generally higher than those of MoS_2 nanocomposites, the only exception being the nanocomposite with C_3N_4. From this we can say that the photochemical HER activity of 2H-MoS_2 and 2H-$MoSe_2$ can be significantly improve by covalent cross-linking with other 2 D materials.[12–15]

Stable 1T-form of bulk MoS_2 and $MoSe_2$ could be also synthesized by solvothermal and hydrothermal routes. The synthesized samples were characterized by Raman spectroscopy. The Raman spectrum of 1T-MoS_2 synthesized via a solvothermal (DMF) route is shown in **Figure** 5a. The characteristic J1, J2 and J3 bands of 1T-MoS2 are at 147, 2 36 and 336 cm^{-1} respectively. The A_{1g} band characteristic of the 2H-phase has a very low intensity (**Figure** 9a) suggesting that the sample consists predominantly of the 1T phase. The intensity of the A_{1g} peak increases over long periods indicating slow conversion from 1T to 2 H-phase (**Figures** 9a and 10). The Raman spectrum of 1T-$MoSe_2$ exhibits the characteristic J1, J2 and J3 bands appear at 118, 154 and 221 cm^{-1}, respectively. The 1T-phase of $MoSe_2$ is stable for 2 weeks without any significant change in the relative Raman band intensities (**Figure** 9b). There was no appearance of the A_{1g} band of the 2H-form during this period. The 1T-phases of MoS_2 and $MoSe_2$ obtained via hydrothermal means also show the characteristic Raman bands. Thus, 1T-MoS_2 exhibits J1, J2 , J3 bands at 154, 244 and 340 cm^{-1} and the intensity of the A_{1g} band due to the 2H phase is insignificant.

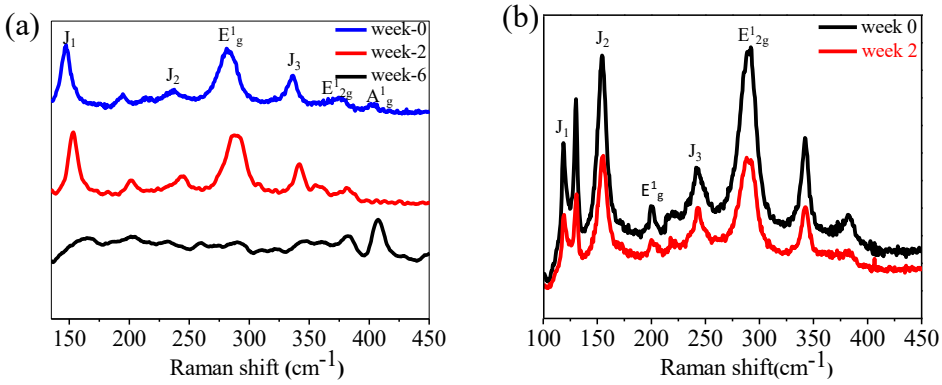

Figure 9: Raman Spectra of (a) 1T-MoS_2 and of (b) 1T-$MoSe_2$ respectively synthesized solvothermally recorded after different periods to demonstrate stability of the 1T-phase.

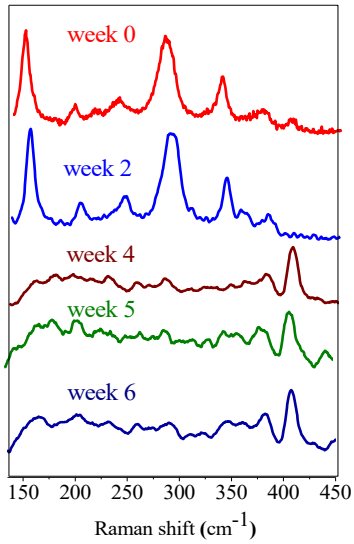

Figure 10: Raman Spectra of 1T-MoS_2 recorded for 6 weeks. The conversion from 1T to 2H-phase appear in 4 weeks.

After 2 weeks, we observed no change in the relative intensities of the bands indicating stability of the 1T-phase (**Figure** 11a). The Raman spectrum of the 1T-phase of $MoSe_2$ prepared hydrothermally shows the J1, J2 and J3 bands at 118, 154 and 222 cm^{-1}, respectively. Similar to $MoSe_2$ synthesized via solvothermal route, we see no A_{1g} band due to the 2H phase (**Figure** 11b). The relative peak

intensities of the 1T phase do not change over a period of one week.

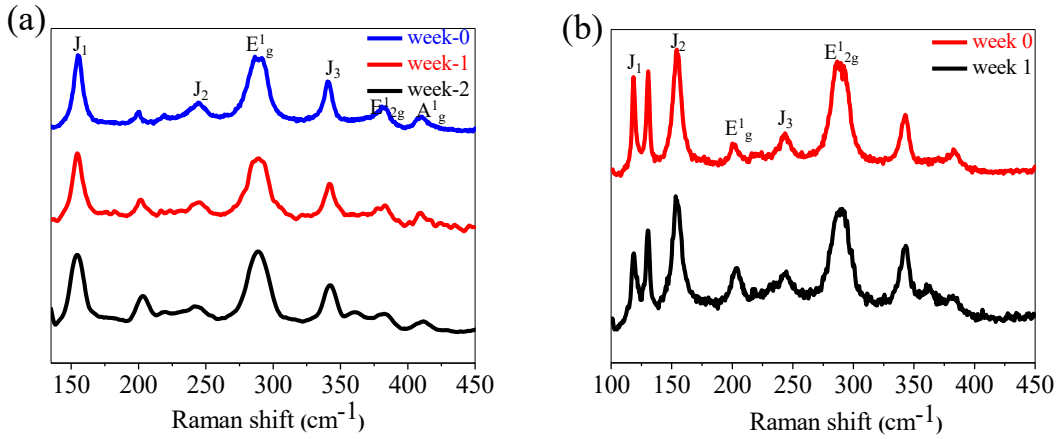

Figure 11: Raman Spectra of (a) 1T-MoS_2 and of (b) 1T-$MoSe_2$ respectively synthesized hydrothermally recorded after different periods to demonstrate stability of the 1T-phase.

We have studied the HER activity of both 1T-MoS_2 and 1T-$MoSe_2$ synthesized by solvothermal and hydrothermal routes in the presence of Eosin Y dye in aqueous solution triethanolamine (15% v/v). The activity of 1T-MoS_2 and 1T-$MoSe_2$ synthesized in DMF had an activity of 31700 and 57500 $\mu molg^{-1}h^{-1}$ (**Figure** 12a), the activity of $MoSe_2$ being considerably higher. Due to similar hydrogen binding energy of Mo and Se, both atoms can act as a hydrogen evolution site in contrast to MoS_2 where only Mo atoms are the HER site.[10] The activity of the 1T-MoS_2 was studied over a period of 6 weeks. The activity of MoS_2 31700, 37700, 37000 and 28000 $\mu molg^{-1}h^{-1}$ for 0, 2 , 4 and 6 weeks, respectively (**Figure** 12b and **Table** 2)

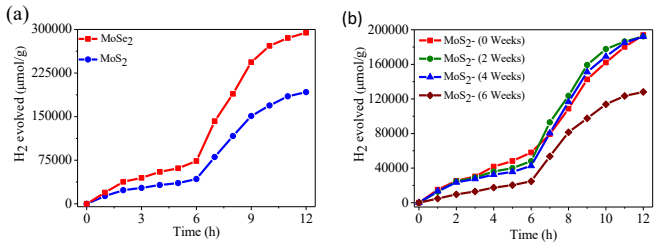

Figure 12: Comparison of hydrogen evolution activity of (a) 1T-MoS_2 and 1T-$MoSe_2$ synthesized solvothermally and (b) over a period of 6 weeks in the case of MoS_2.

	Before Induction Period* (µmoles g^{-1} h^{-1})	After Induction period# (µmoles g^{-1} h^{-1})
MoS_2		
0 Weeks	12600	31700
2 Weeks	12400	37700
4 Weeks	11700	37000
6 Weeks	4800	28000
$MoSe_2$	12700	57500

* First six hours, # next six hours on further addition of dye

Table 2: Comparison of photochemical hydrogen evolution activity of 1T-MoS_2 as a function of time and $MoSe_2$.

We observe a decrease in the activity of the samples after 6 weeks due to slow conversion of the 1T to the 2H-phase as observed from Raman spectra. Stable HER evolution over long periods is observed from cycling studies. HER activity of the 1T-phases of MoS_2 and $MoSe_2$ synthesized via hydrothermal means was 17000 and 35000 $\mu molg^{-1}h^{-1}$, respectively (**Figure** 13a). Similar to the 1T-samples synthesized in DMF, we observe higher activity in the case of $MoSe_2$. The activity of 1T-MoS_2 was studied for two weeks. The activity after 2 weeks was 1400 $\mu molg^{-1}h^{-1}$ (**Figure** 13b).

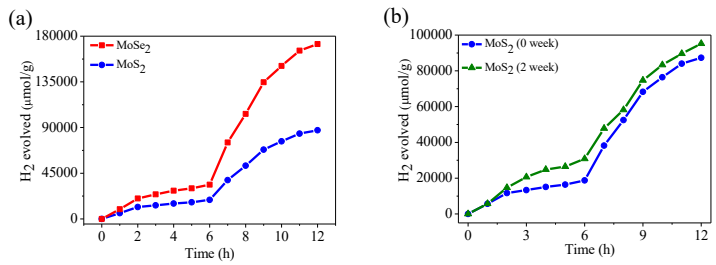

Figure 13: Comparison of hydrogen evolution activity of (a) 1T-MoS_2 and 1T-$MoSe_2$, synthesized using a hydrothermal route, and (b) over a period of 2 weeks in the case of 1T-MoS_2.

We have compared the photochemical activity of the 1T phase obtained by solvothermal and hydrothermal methods with that synthesized from Li-intercalation and exfoliation in **Table** 3 . The 1T phase from solvothermal and hydrothermal methods show comparable photocatalytic activities and are suitable for practical use. In this aspect, 1T phases are superior to the nanocomposites obtained by covalent linking of layer structures.

	Synthetic method	Activity (μmoles g^{-1} h^{-1})	TOF (h^{-1})
1T- MoS_2	(a) Li-intercalation and exfoliation[5]	30,000	4.8
	(b) $MoCl_5$ + Thioacetamide in DMF, 200 °C (Solvothermal)	37,000	6.0
	(c) $Na_2MoO_4.2H_2O$ + Thiourea in water + propionic acid, 200 °C (Hydrothermal)	16,000	2.5
1T- $MoSe_2$	(a) Li-intercalation and exfoliation[5]	75,000	19.0
	(a) $MoCl_5$ + Selenourea in DMF, 200 °C (Solvothermal)	57,500	14.6
	(c) $Na_2MoO_4.2H_2O$ + Selenourea in water + propionic acid, 200 °C (Hydrothermal)	35,000	8.9

Table 3: Comparison of photochemical hydrogen evolution by 1T-MoS_2 and 1T-$MoSe_2$ synthesised by different methods.

3.4 Conclusions

The present study shows that it is possible to utilize the semiconducting 2H phases of MoS_2 and $MoSe_2$ as photocatalysts for HER by forming covalently linked nanocomposites with other 2D materials such as BC_7N or by self-assembly. The photochemical activity of covalently cross-linked nanocomposites is sufficiently high for possible practical use (though not as high as that of the 1T phases). The performance of MoS_2 and $MoSe_2$ nanocomposites with a borocarbonitride such as BC_7N is noteworthy. It is interesting that by linking MoS_2 and $MoSe_2$ to another 2D material one can enhance the photochemical

activity substantially. Cross-linking of 2H-MoS_2 and $MoSe_2$ with BC_7N and C_3N_4 is likely to involve charge transfer between the two heterolayers.

We were able to synthesize the stable 1T-MoS_2 and $MoSe_2$ by simple hydrothermal and solvothermal methods. The 1T samples so prepared are stable (upto 2–4 weeks) unlike those obtained by Li-intercalation followed by exfoliation. Photochemical HER activity of 1T MoS_2 and 1T $MoSe_2$ is remarkable and can be of practical use.

References

[1] O. US EPA, Greenhouse Gas (GHG) Emissions. *US EPA* **2015**.

[2] N. Abas, A. Kalair, N. Khan, *Futures* **2015**, *69*, 31.

[3] Energy and Air Pollution - World Energy Outlook 2016 Special Report, **2016**, 266.

[4] U.S. Department of Energy Hydrogen and Fuel Cell Technology Overview, **2018**, 42.

[5] J. A. Turner, *Science* **2004**, *305*, 972.

[6] P. Millet, R. Ngameni, S. A. Grigoriev, N. Mbemba, F. Brisset, A. Ranjbari, C. Etiévant, *Int. J. Hydrog. Energy* **2010**, *35*, 5043.

[7] J. Yu, L. Qi, M. Jaroniec, *J. Phys. Chem. C* **2010**, *114*, 13118.

[8] X. Wang, K. Maeda, A. Thomas, K. Takanabe, G. Xin, J. M. Carlsson, K. Domen, M. Antonietti, *Nat. Mater.* **2008**, *8*, 76.

[9] C. N. R. Rao, S. R. Lingampalli, S. Dey, A. Roy, *Philos. Trans. R. Soc. Math. Phys. Eng. Sci.* **2016**, *374*, 20150088.

[10] U. Gupta, B. S. Naidu, U. Maitra, A. Singh, S. N. Shirodkar, U. V. Waghmare, C. N. R. Rao, *APL Mater.* **2014**, *2*, 092802.

[11] Z. Lei, J. Zhan, L. Tang, Y. Zhang, Y. Wang, *Adv. Energy Mater.* **2018**, *8*, 1703482.

[12] K. Pramoda, U. Gupta, I. Ahmad, R. Kumar, C. N. R. Rao, *J. Mater. Chem. A* **2016**, *4*, 8989.

[13] K. Pramoda, U. Gupta, M. Chhetri, A. Bandyopadhyay, S. K. Pati, C. N. R. Rao, *ACS Appl. Mater. Interfaces* **2017**, *9*, 10664.

[14] K. Pramoda, M. M. Ayyub, N. K. Singh, M. Chhetri, U. Gupta, A. Soni, C. N. R. Rao, *J. Phys. Chem. C* **2017**, *122*, 13376.

[15] N. K. Singh, K. Pramoda, K. Gopalakrishnan, C. N. R. Rao, *RSC Adv.* **2018**, *8*, 17237.

[16] T. P. Nguyen, S. Choi, J.-M. Jeon, K. C. Kwon, H. W. Jang, S. Y. Kim, *J. Phys. Chem. C* **2016**, *120*, 3929.

[17] C. Tsai, K. Chan, F. Abild-Pedersen, J. K. Nørskov, *Phys Chem Chem Phys* **2014**, *16*, 13156.

[18] K. Srinivasu, B. Modak, S. K. Ghosh, *J. Phys. Chem. C* **2014**, *118*, 26479.

[19] Y. Zheng, Y. Jiao, Y. Zhu, L. H. Li, Y. Han, Y. Chen, A. Du, M. Jaroniec, S. Z. Qiao, *Nat. Commun.* **2014**, *5*.

[20] N. kumar, K. Moses, K. Pramoda, S. N. Shirodkar, A. K. Mishra, U. V. Waghmare, A. Sundaresan, C. N. R. Rao, *J. Mater. Chem. A* **2013**, *1*, 5806.

[21] M. Barua, M. B. Sreedhara, K. Pramoda, C. N. R. Rao, *Chem. Phys. Lett.* **2017**, *683*, 459.

[22] W. Yang, L. Gan, H. Li, T. Zhai, *Inorg. Chem. Front.* **2016**, *3*, 433.

[23] B. Radisavljevic, A. Radenovic, J. Brivio, V. Giacometti, A. Kis, *Nat. Nanotechnol.* **2011**, *6*, 147.

[24] P. Vishnoi, A. Sampath, U. V. Waghmare, C. N. R. Rao, *Chem. - Eur. J.* **2016**, *23*, 886.

[25] M. Chhetri, S. Maitra, H. Chakraborty, U. V. Waghmare, C. N. R. Rao, *Energy Env. Sci* **2016**, *9*, 95.

[26] Q. Liu, Q. Fang, W. Chu, Y. Wan, X. Li, W. Xu, M. Habib, S. Tao, Y. Zhou, D. Liu, T. Xiang, A. Khalil, X. Wu, M. Chhowalla, P. M. Ajayan, L. Song, *Chem. Mater.* **2017**, *29*, 4738.

[27] Z. Liu, Z. Gao, Y. Liu, M. Xia, R. Wang, N. Li, *ACS Appl. Mater. Interfaces* **2017**, *9*, 25291.

[28] A. Zheltikov, *J. Raman Spectrosc.* **2005**, *36*, 834.

[29] P. Tonndorf, R. Schmidt, P. Böttger, X. Zhang, J. Börner, A. Liebig, M. Albrecht, C. Kloc, O. Gordan, D. R. T. Zahn, S. M. de Vasconcellos, R. Bratschitsch, OSA, **2013**.

[30] K. Pramoda, R. Kumar, C. N. R. Rao, *Chem. - Asian J.* **2015**, *10*, 2147.

[31] U. Maitra, U. Gupta, M. De, R. Datta, A. Govindaraj, C. N. R. Rao, *Angew. Chem. Int. Ed.* **2013**, *52*, 13057.

CHAPTER 3

Atomic layer deposition of TiS_2-nanowall networks with superior performance in thin film rechargeable batteries

SUMMARY

TiS_2 thin films have been grown by Atomic Layer Deposition (ALD) using $TiCl_4$ and H_2S as Ti and S precursors respectively. The thin films have been characterized by various microscopic and spectroscopic techniques. Interestingly, the films show nanowall network morphology and exhibit a high surface to volume ratio irrespective of the underlying substrate. The films grown on c-sapphire are crystalline in nature and those on other substrates are amorphous. Nanowall networks grown directly on stainless steel substrate show high performance in Na-ion/Li-ion batteries with TiS_2 as the active electrode without any binder and conductive matrix.

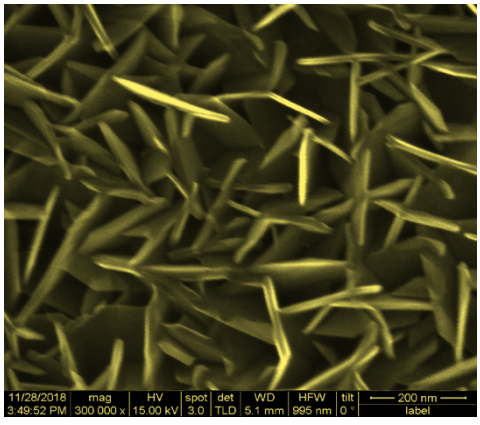

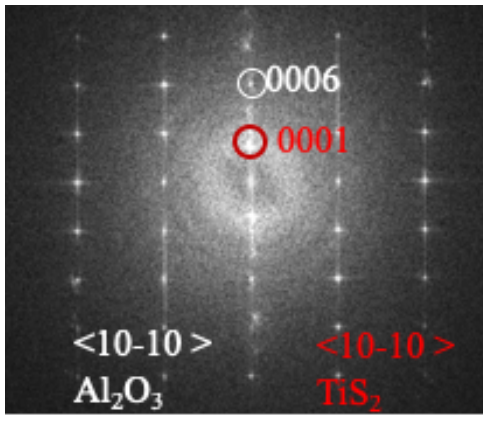

Introduction

Atomic Layer deposition (ALD) was introduced as atomic layer epitaxy (ALE) by Suntola and Antson in 1977, depositing ZnS for flat panel displays.[1] Further ALE processes were developed for a wide range of materials like metals, metal oxides and metal sulfides.[2,3] Past 1990s the demand for ALD have been grown significantly due the advancement in the instrumentation. ALD is one of the most powerful techniques to grow very thin conformal thin films with control of thickness and composition upto atomic level.[3–6] Other advantages include growth of thin films at lower temperatures, pin-hole free and self- limiting growth.[4] ALD is a Chemical Vapor Deposition (CVD) technique which depends on the surface saturating irreversible chemisorption of gaseous precursor on solid surface.[7] The distinct feature of ALD compared to CVD is the sequential exposure of precursors and reactants. Under such conditions the growth is uniform, and the thickness of the film increases steadily in each growth cycle. One complete ALD cycle takes place in four steps which are shown in **Figure 1**[8]. In the first step, the precursor is exposed to the surface of substrate which chemisorb there irreversibly leaves by-product and terminates the surface with new reactive groups, in second step the excess precursor and un-reacted precursors are purged out. In third step exposure of the reactant species, generally reagents, which chemically reacts with the surface groups of the precursor and in fourth step again purging of the reactant and by-products with the inter gas. This cycle can be repeated many times to get desired film thickness depending on the growth rate. The time for one complete cycle can vary from milli-seconds to seconds depending on the chemistry of precursor and reagent used in deposition and it may deposit sub monolayer to a monolayer in one cycle.

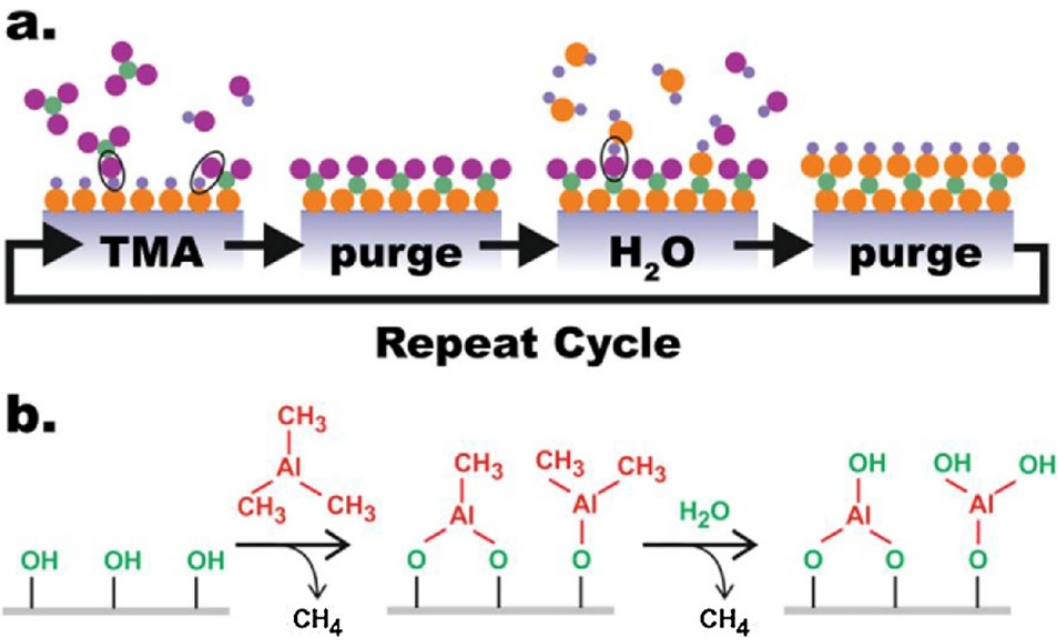

Figure 1: Schematic diagram of ALD for depositing Al_2O_3 via trimethylaluminum (TMA) and water (H_2O). (a) exposure scheme of one ALD cycle. (b) idealized stoichiometry of surface reaction. Reproduced with permission from ref[8]. © 2018 Elsevier B.V.

The thickness of the film can be directly controlled by controlling the number of reaction cycles, therefore enabling the controlled growth at monolayer level. As a result, ALD film growth is not flux dependent as is the case with the Physical Vapor Deposition (PVD) and CVD. Irreversibility and self-limiting nature of ALD lead to stoichiometric films where the same amount of material gets adsorbed independent of the exposure time shape of the substrate, and amount of the material adsorbed during the growth.[7,9] Another important feature of ALD is the growth is weakly dependent on the temperature in ALD temperature window. ALD temperature window is one of the most important parameter because a real ALD process occurs only when the growth temperature is placed within a precise range i.e., ALD temperature window.

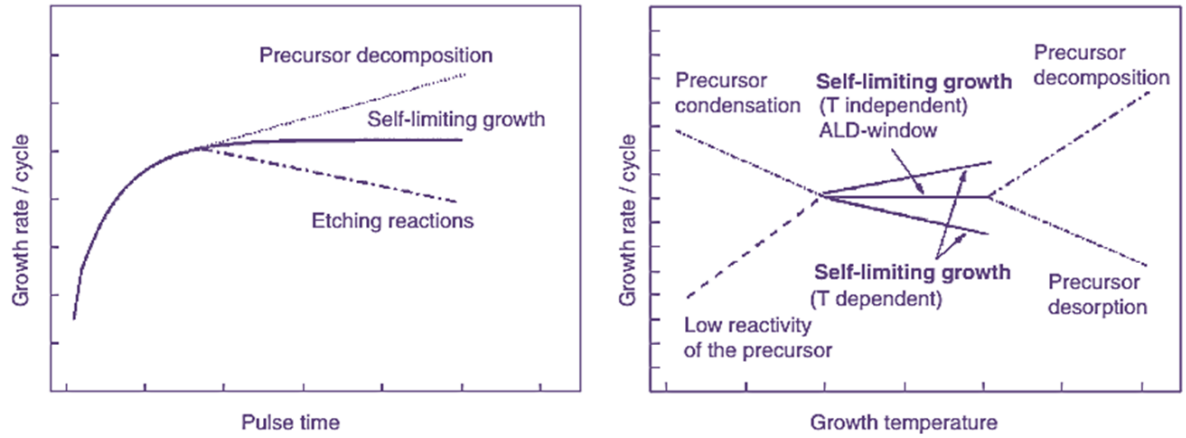

Figure 2: Schematic diagram of possible behavior of ALD growth rate versus precursor pulse time and temperature showing the ALD window. Reproduced with permission ref.[10] © Royal Society of Chemistry, 2009

Figure 2 clearly shows the nearly ideal, non-ideal behavior regions of ALD growth. ALD temperature window corresponds to the range in which growth rate is fairly stable with in experimental errors. As we can see from **Figure** 2, The growth rate outside the ALD temperature window can be affected due to undesired chemical and physical processes. The lower growth rate below the window can be attributed to insufficient thermal energy supplied to the molecules and higher rate to the condensation of precursor molecules. Change in growth rate within the window is very less and it can be due to the thermally promoted gas phase reactions. For a good ALD deposition one should first optimize the temperature window, which depends on the nature of precursor. The different precursors of a same metal may have different temperature window. Once the temperature window and pulsing time of precursor is optimized, then the growth rate should be constant, and the thickness of the film should vary linearly with the number of cycles. If the growth rate is stable and the film thickness is uniform on substrate one can achieve extremely conformal ultrathin films of high aspect ratio with steady thickness. ALD growth may not be possible with many precursors used in CVD due to their inability to show self-limiting reactions.

There are large number of areas where ALD has potential application because of advantages it possesses over other methods for growth of thin films. ALD has been successfully employed in semiconductor industry, fabrication of electrochemical devices, catalytic surfaces, battery electrodes[11,12] and many other areas.

In recent years, ALD of sulfide materials has been extended for photonic and energy applications.[13] Like earth-abundant metal sulfides can be potential alternatives to silicon in solar cells, they can be very good catalyst in various processes, good electrode and electrolyte for energy storage applications. In this work our material of interest is Titanium Sulfide (TiS_2). TiS_2 is a transition metal dichalcogenide that crystallizes in hexagonal (hcp) structure, similar to CdI_2 where half of the octahedral site are filled with Ti^{4+} and which in turn is surrounded by six sulfide anions in an octahedral environment. The layers of TiS_2, thus formed, consist of covalent Ti-S bonds and individual layers of TiS_2 are bound together by intermolecular van der waals forces.[14] These stacked layers open the possibility of ion intercalation which can be used as a hydrogen storage and electrode material in Li, Na and Mg ion batteries.

Different methods have been employed for the synthesis of TiS_2 in both the forms powder and thin films. Various vacuum deposition techniques like Metal Organic Chemical Vapor Deposition (MOCVD), Atmospheric Pressure Chemical Vapor Deposition (APCVD) and plasma CVD have been already explored for thin films of TiS_2. There are ALD reports for the synthesis of TiS_2[15,16] but most of them are at temperatures higher than 300 °C and for applications like solar cell. In this work we have successfully grown crystalline TiS_2 thin films nanowall networks on c-sapphire (0001) by thermal ALD without post-annealing treatment. The nanowall network has been characterized by various spectroscopic and microscopic techniques. The nanowalls consist TiS_2 nanosheet with a high surface to volume ratio. These nanowalls showed inclined vertical growth. We

also explored TiS_2 thin film as an electrode material for Li and Na ion batteries. We have found good cyclability and stability in the case of alumina coated TiS_2 thin films under the varying current densities for Li and Na ion batteries. All these measurements were done taking TiS_2 as an electrode without any binder and conductive matrix.

Experimental

Deposition of crystalline TiS2 thin films using atomic layer deposition

For this study we have grown crystalline TiS_2 thin films having nanowall network by ALD on single crystalline c-sapphire (0001), Si (100), SiO_2/Si, stainless steel (ss) substrates using a flow type ALD reactor (Beneq, TFS 200, Finland Oy). Prior to deposition all the wafers were cleaned thoroughly by chemical treatment using H_2SO_4 and H_2O_2 in the ratio 4:1 at 120 °C followed by ultrasonication in acetone and isopropanol and dried under ultra-pure nitrogen. High purity Titanium tetrachloride ($TiCl_4$, Alfa Aesar 99.99%) as precursor for Ti and hydrogen sulfide (H_2S, Bhuruka gases, 97.5%) as a precursor for S were employed. Ultra-pure Nitrogen (Chemix, 99.9995) was used as a carrier and purging gas at the flow rate of 600 sccm throughout the deposition. The chamber and reactor were pumped down to 10 and 1 mbar respectively before the starting the deposition. The reaction chamber was heated to 300 °C and hold 30 minutes for temperature stabilization. $TiCl_4$ precursor was kept in a liquid bubbler and maintained at 20 °C. The precursor is allowed to enter the reactor on its own vapor pressure without any booster steep. The films were deposited by sequential pulsing of $TiCl_4$ and H_2S. The chamber pressure was almost constant throughout the deposition whereas variation in the reactor pressure between 1-3 mbar was observed during the pulsing and purging of the precursor. To ascertain the self-limiting nature of ALD process and ALD temperature window, the depositions are carried out at different reactor temperatures and pulse and purge times. The

temperature window for ALD growth was tested between 150 and 300 °C. The films appear to grow more uniformly at 300 °C without and residual chlorine. The optimized pulsing and purging times for $TiCl_4$ were 400 ms and 3s respectively, whereas the pulsing and purging times for H_2S were 1s and 3s. One complete ALD cycle for TiS_2 growth was pulse $TiCl_4$/purge//pulse H_2S/purge for 200 ms/3 s//1 s/3 s. The deposition was carried out for 500, 1000, 1500 and 2000 cycles at 300 °C and the films cooled down to room temperature under vacuum under constant flow of N_2. The as-obtained films appear black in color and used for further microscopic and spectroscopic characterization without post annealing.

Characterization of TiS_2 thin films

TiS_2 thin films X-ray diffraction (XRD) patterns of the as-deposited films were recorded with a Panalytical Empyrean diffractometer with θ-2θ scan using monochromatic Cu Kα1 radiation (λ = 1.5404Å) to confirm the crystallinity. Field emission scanning electron microscope (FESEM) Nova NanoSEM 600 FESEM equipped with an Energy Dispersive X-ray (EDX) analysis system (FEI Company) was employed to ascertain the film thickness and surface morphology. Raman optical modes of TiS_2 were recorded in using a 514 nm Argon (Ar) laser with a Jobin Yvon LabRam HR spectrometer in backscattering geometry. X-ray photoelectron spectra (XPS) were recorded using an Omicron nanotechnology spectrometer with Mg Kα X-ray source (E = 1253.6 eV). Initially, sample was thinned down to few micrometres (mm) by mechanical polishing and then perforation was done using ion milling using Ar gas. This perforation provides a thin layer (few nm thickness), which is electronically transparent to transmission electron microscopy (TEM). Polishing was done carefully so that the weak wan der waals layers of TiS_2 do not delaminate from the substrate. ion milling. Cross-sectional high-resolution TEM (HRTEM) was performed using double aberration corrected FEI TITAN 80−300 kV operated at 300 kV.

Electrode fabrication and electrochemical measurements

All the electrochemical measurements were performed in a coin cell configuration of TiS_2 electrode cast on ss spacer disk. The pure metals (Li and Na) was used as both reference and counter electrode separated by electrolyte-soaked quartz separator. The three electrolytes used in present study were prepared by dissolving 1M $LiPF_6$, $LiClO_4$ and $NaClO_4$ in equimolar (1:1) ethyl carbonate (EC) and dimethyl carbonate (DMC) solutions. The cyclic voltammogram (CV) are recorded in a potential window 0.5-3.0 V with 0.01 mV s^{-1} on CH instrument (CH03).

Results and discussion

TiS_2 thin films having nanowall network of various thicknesses have been grown on the c-sapphire (c-Al_2O_3), ss, silicon (Si), silicon-dioxide/silicon (SiO_2/Si) and quartz by thermal ALD using $TiCl_4$ and H_2S as the precursors for Ti and S respectively were characterized by various spectroscopic and microscopic techniques and also performed the Li and Na ion batteries studies. ALD temperature window and other parameters were optimized for a self-limiting surface saturation reaction with large area films of uniform thickness. After trying different temperatures and substrates. We obtained crystalline thin films on c-sapphire and a growth temperature of 300 °C. On repeating the growth, similar trends were observed which indicates the uniformity in growth. Thickness of the film could not be determined precisely due to network type morphology. To stop the intermixing of precursors and back-etching reactions from by-products, we kept purging time sufficiently long. We observed uniform growth with the same morphology at 300 °C, even for a higher pulsing time for $TiCl_4$ and H_2S without any chlorine contamination

The crystallinity of thin films was established by XRD studies. The films on c-sapphire were crystalline without any post-annealing. **Figure** 3a shows the XRD spectra of TiS_2 grown on c-sapphire at 300 °C for 2000 ALD cycles with preferred orientation of <0001> (TiS_2) // (0001) <Al_2O_3>. The presence of only (001) reflections at 15.6° of TiS_2 in diffraction pattern suggests ordered growth of TiS_2 on c-sapphire. The broader and weaker reflections of TiS_2 may indicate that there might be some amorphous regions in the film along with the crystalline regimes which can be attributed to lower growth temperature. The thickness of the films is of several nanometers which might affect the intensity and width of the reflections. From XRD studies, the crystal geometry relation between the substrate and film is found to be <0001> (TiS_2) // (0001) <Al_2O_3>. TiS_2 films deposited on other substrates such as ss, Si, SiO_2/Si and quartz at 300 °C were amorphous in nature but have the same nanowall network. The crystallinity on c-sapphire may arises due to the same hexagonal crystal geometry with less lattice mismatch of the grown films with underlying substrate.

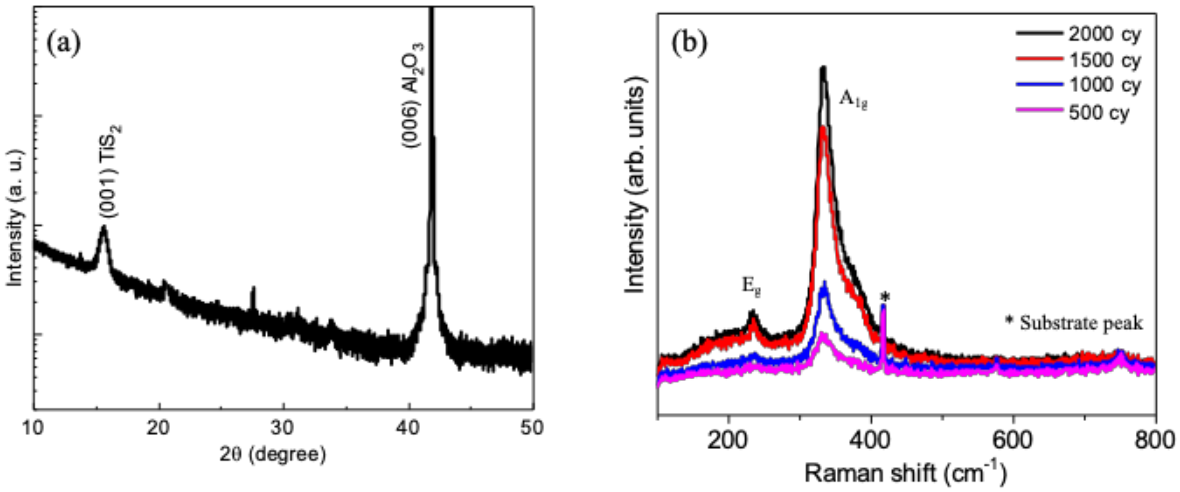

Figure 3: (a) XRD pattern of TiS_2 thin films for 2000 ALD cycles on c-sapphire substrate. (b) Raman spectra of TiS_2 thin films grown on c-sapphire substrate of various thickness. (* indicates the peak corresponding to the substrate.)

The optical properties of TiS_2 thin films of varying thickness under ambient conditions were investigated using Raman spectroscopy (excitation using 514 nm laser) **Figure** 3b sows the Raman spectra of TiS_2 thin films on c-sapphire at 300 °C for 500, 1000, 1500, 2000 ALD cycles. The Raman spectra display significant signals due to the in-plane E_g and out-of-plane A_{1g} optical phonon modes. Intensities of both the signal clearly depends on the thickness of the film.

XPS has been done to understand the bonding nature of grown films. **Figure** 4 shows the core level XP spectra for TiS_2 thin films grown on c-sapphire for 2000 cycles. We observed all the characteristics signals corresponding to Ti and S.

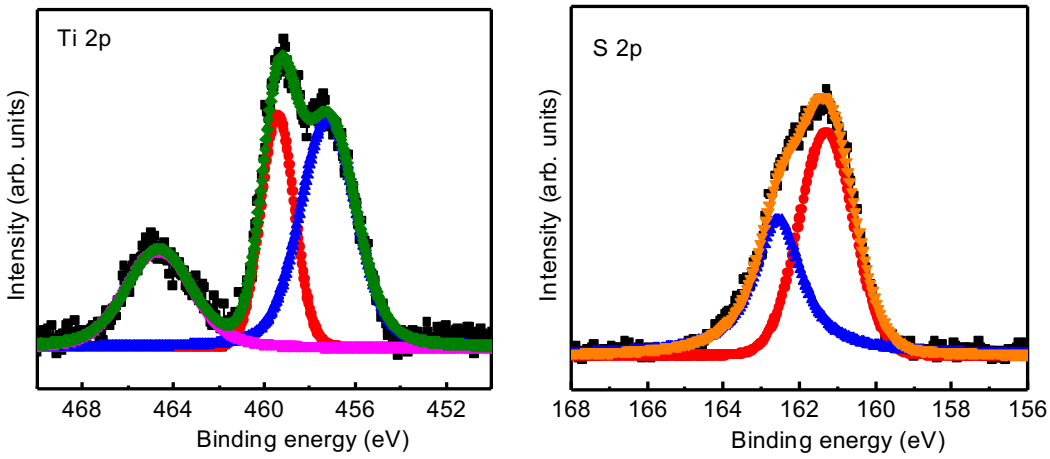

Figure 4: Core-level XP spectra of Ti (2p) and S (2p) of TiS_2 film grown for 2000 ALD cycles on c-sapphire.

The surface morphology of TiS_2 thin films were examined by FE-SEM. **Figure** 5a-d shows the in-plane view of TiS_2 films grown on c-sapphire for 2000 ALD cycles. The vertically aligned nanowall network morphology has been observed by the top view images and are observed to be uniformly distributed over a large area. Sheets of TiS_2 grown vertically and combined with the edges of adjoining nanosheets making an expansive nanowall network. The growth of the individual nanowall is regular and uniform throughout. The thickness of each nanowall is nearly same across the network. The network shows the presence of pores or

voids in between the nanowalls. **Figure** 5e shows the EDAX spectra of TiS_2 which confirms the presence of Ti and S without any Chlorine contamination.

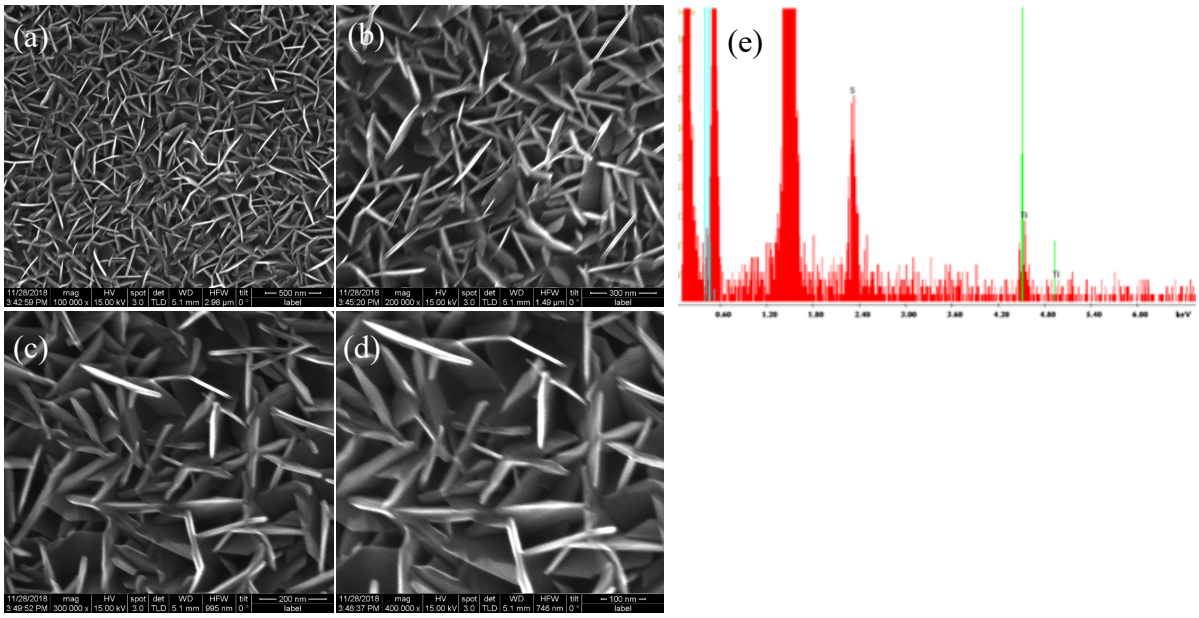

Figure 5: (a-d) shows the SEM images of TiS_2 on c-sapphire for 2000 ALD cycles. (e) shows the EDAX spectra of TiS_2 on c-sapphire for 2000 ALD cycles.

In order to understand the crystalline growth pattern. TiS_2 films grown on c-sapphire are characterized though cross-section TEM. The TEM and HRTEM studies were done by Usha Bhat and Prof. Ranjan Datta. To acquire high quality images the films were mechanically polished before the characterization. HRTEM images reveal that up to few nanometers (5-10) on the substrate TiS_2 is polycrystalline or amorphous in nature and then crystalline ordered van der Waals layers of TiS_2 are formed above that. The number of layers vary from region to region, approximately 10 to 15 layers with the interlayer distance of 5.7 Å. **Figure** 6 (i) region (a), (b) confirms the layered growth of TiS_2. **Figure** 6 (i) region (c) shows the amorphous region growth of TiS_2 on sapphire. **Figure** 6 (i) region (d) film-substrate interface. **Figure** 6 (i) region (e) shows the bare substrate **Figure** 6 (iv) corresponds to the fast Fourier transform (FFT) of substrate, interface and layers together. The epitaxial relationship is <0001> Al_2O_3 // <0006> TiS_2 and <10-10> Al_2O_3 // <10-10> TiS_2.

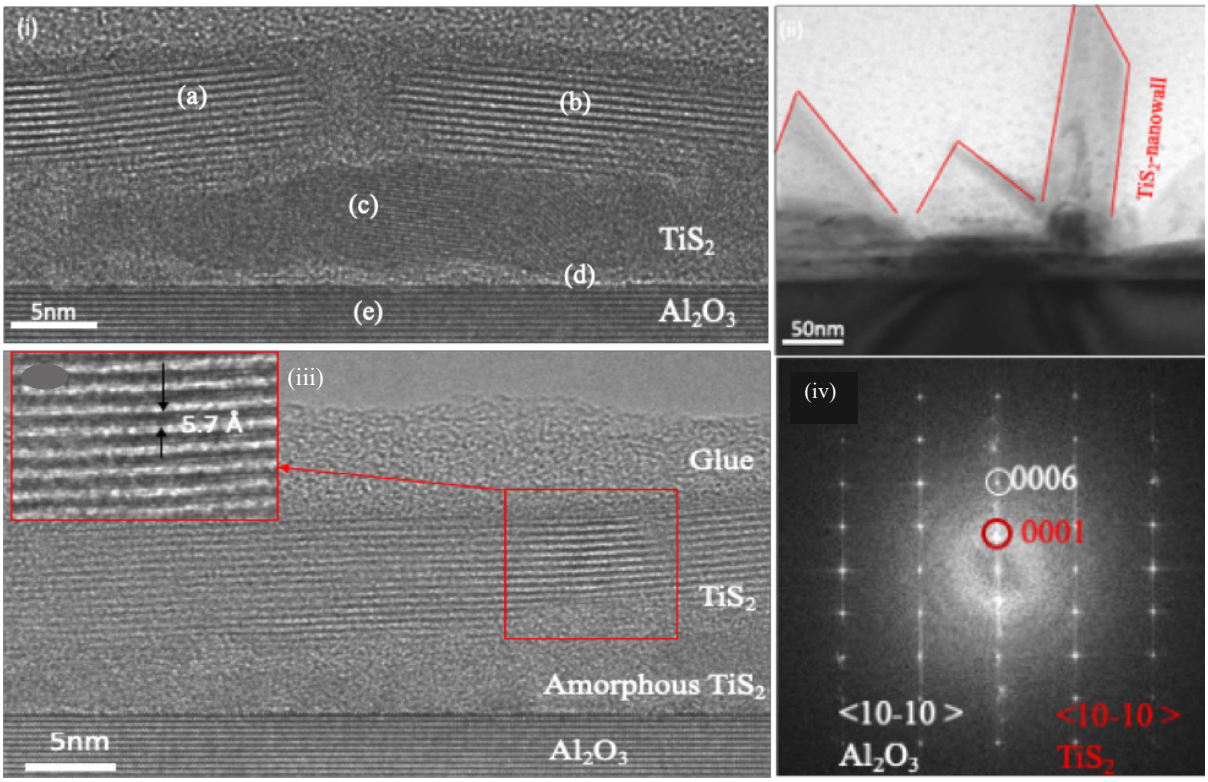

Figure 6: (i) HRTEM of TiS_2 on c-sapphire for 2000 ALD cycles at 300 °C showing different regions (a-b) vertical growth of TiS_2 layers, (c) the amorphous regions of TiS_2 (d) film-substrate interface and (e) the bare substrate. 6 (ii) Low resolution TEM showing the vertical nanowalls of TiS_2. 6 (iii) Amorphous and layered structure of TiS_2 with interlayer distance of 5.7 Å as shown in inset. 6 (iv) FFT of the film-substrate interface shows the epitaxial relationship of <001> Al_2O_3 // <0001> TiS_2 and <10-10> Al_2O_3 // <10-10> TiS_2.

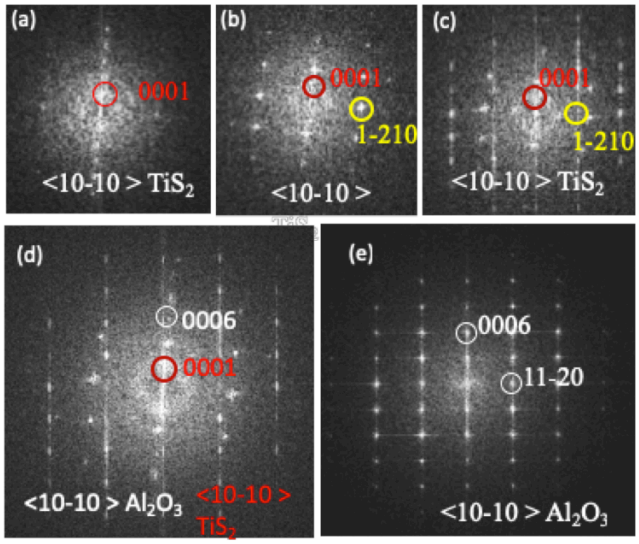

Figure 7: FFTs of all five regions a, b, c, d, e, which shown in Figure 6 (i)

Figure 7 shows the FFT of the all the regions a, b, c, d, e, which were shown in Figure 6 (i). confirming all the details from **Figure** 6 (i). However, HRTEM images show roughness of the films due to regions of the films turning vertical. The reflections corresponding to the vertical growth regions are not observed in the X-ray diffraction pattern due to the restricted geometry.

The controlled synthesis conditions in ALD led to the desired TiS_2 phase formation. The phase diagram of Ti-S includes many stoichiometric ratios, the stable form being TiS_2. Under certain conditions, TiS_2 may convert to TiS via Ti_2S_3, an intermediate phase. However, from intercalation chemistry point of view TiS_2 structure is more promising.[17] Excess of titanium can cause pinning of the sulfide layers which will reduce the diffusion of the alkali ions and at the same time occupy some of the sites where the Li^+ ion would otherwise reside.[18] For structural characterization of ALD deposited sulfide samples, the sample was also deposited on alumina substrate under the same condition. **Figure** 3a shows the observed XRD pattern of sample, with the highest peak from the substrate alumina with (001) reflection at 15.6° of TiS_2 (ICSD #601315). This also confirms the crystallinity of the as grown sample on c-sapphire. The appearance of the intense peak corresponding to the (001) plane for the *P-3m*1 phase suggests orientated growth during the film formation process. Layered TiS_2 structure typically shows characteristic Raman active modes at 232 cm^{-1} (E_g) and 336 cm^{-1} (A_{1g}) for vibrational modes in-plane and perpendicular to plane geometries respectively.[19] With the appearance of the prominent A_{1g} mode suggests that a strong covalent bond exists between the intra-layer atoms and oppositely weak van der Waals force between the layers.

Li^+ and Na^+ intercalation-deintercalation in TiS_2

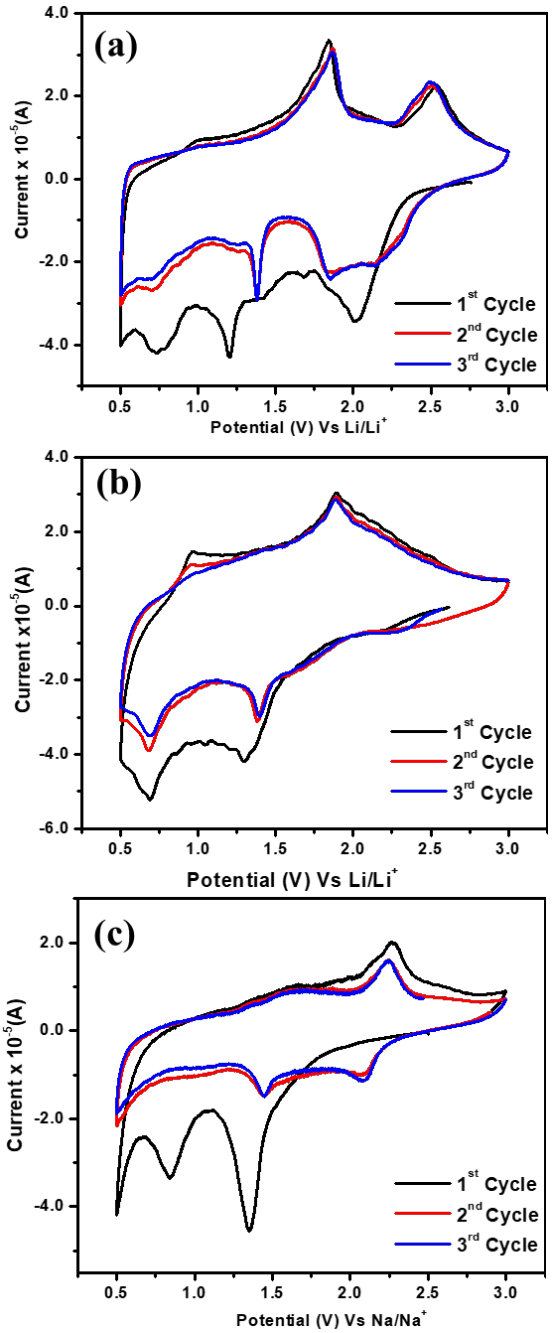

Figure 8: Li intercalation-deintercalation behavior in cyclic voltammogram using Li metal foil as anode in electrochemical potential window 0.5-3.0V with scan rate 0.01 mV s^{-1} using 1M Li ion salts (a) $LiPF_6$ and (b) $LiClO_4$ in EC:DMC electrolytes. (c) Na intercalation-deintercalation behavior of TiS_2 electrode using 1M $NaClO_4$ in EC:DMC electrolyte in 0.5-3.0V potential window with scan 0.01 mV s^{-1} rate using Na metal foil as anode.

The electrochemical studies were performed by Dr. Farheen N. Sayed and Prof. Aninda J. Bhattacharyya. In the discharge-charge profiles of the conducting carbon and binder free depicted in **Figure** 8. The discharge-charge profiles show signature corresponding to the formation of a full range solid solution if $\mathbf{Li_xTiS_2}$ ($0 < x < l$) due to the lithiation and delithiation. The potential window of (0.5-3.0 V) is selected to avoid the conversion reaction: $LiTiS_2 + 3Li^+ + 3e^- \longrightarrow 2Li_2S +$ Ti which is supposed to be dominant process voltages lower than 0.5V.[20] As seen in **Figure** 8a**,** with $LiPF_6$ a more complex and multi-step lithiation process are observed. Four prominent lithiation peaks at 2.01, 1.41, 1.20 and 0.73 V are observed whereas, only two de-lithiation peaks are observed at 1.85 and 2.53 V. The different Li^+-ion intercalation behavior is observed with $LiClO_4$ salt **Figure** 8b. Two distinct lithiation peaks at 1.30 and 0.69 V and de-lithiation peaks at 1.88 and 0.95 V are observed in the 1st cycle. In the subsequent cycles, the intensity of lithiation peak decreases to a greater extent than the delithiation peaks. The magnitude of peak current however, in the two Li-salts are nearly the same. For Na^+-ion intercalation, employing $NaClO_4$ in 1:1 EC:DMC, the cathodic peaks are observed to be same as in case of $LiPF_6$ in EC:DMC. However, the high voltage peak at 2.07 V appear from the second cycle onwards **Figure** 8c. The corresponding anodic peak at 2.27 V is clearly visible in the 1st cycle. The intercalation mechanism of Li^+ and Na^+ ions, irrespective of salt and solvent selection, is attributed to the relatively weakly binding interlayer forces as well as the amenability of the Ti^{4+} centers to reduce to Ti^{3+}. Published reports of Na^+-intercalation in to TiS_2 suggests the appearance of two prominent peaks positioned at 2.07 and 1.35 V. Consistency of the observations reported here with published reports suggests the formation of two different phases upon Na^+ insertion (Na_xTiS_2, where $x=O < x < 0.4$ and Na_xTiS_2, where $x=0.4 < x < 0.8$).[21] The Na^+-intercalation also involves the formation of prismatic coordination which eventually results into two distinct regions solely belonging to Na^+ ion

intercalation. The subsequent cycles show stable values with no trace of 0.84 V lithiation peak.

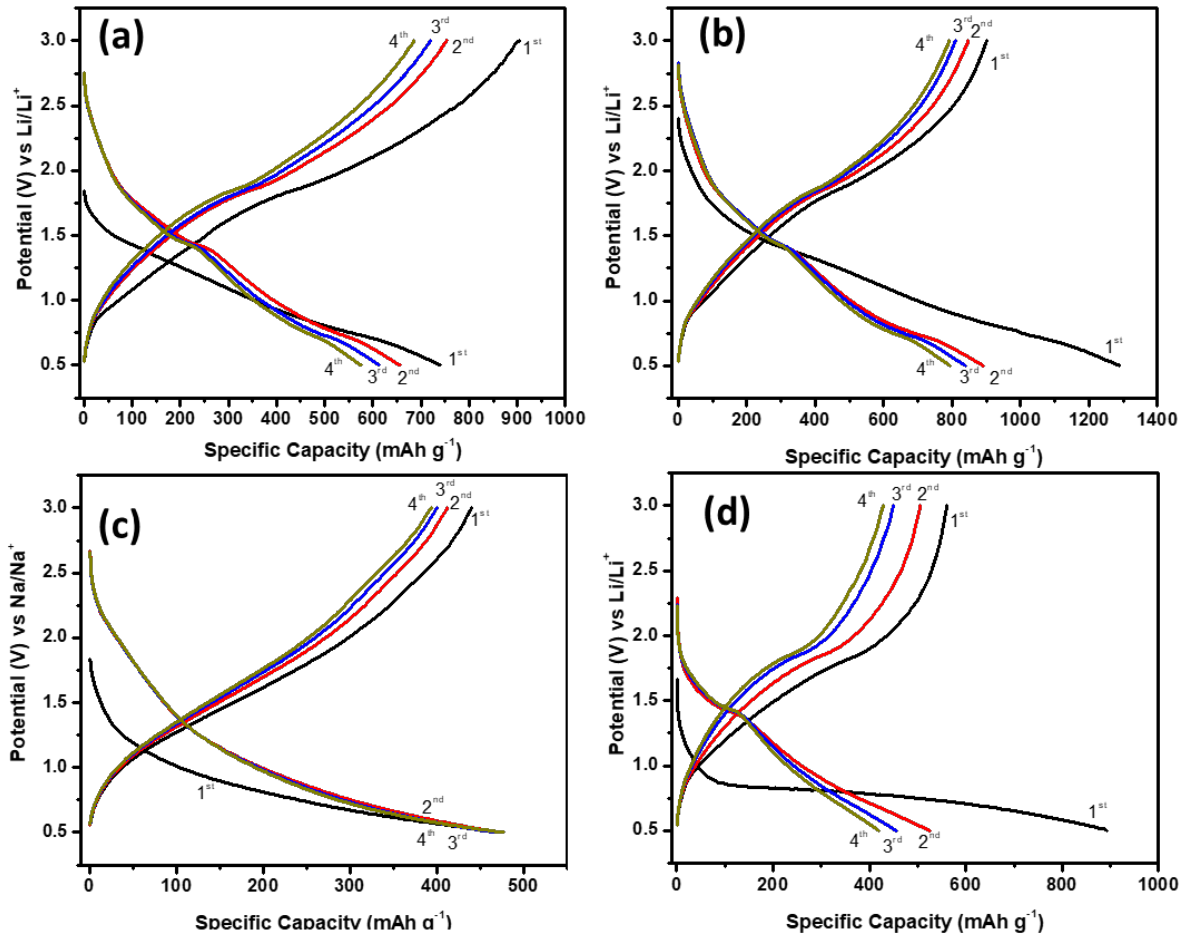

Figure 9: Galvanostatic Discharge-charge curves for TiS_2 with (a) 1M $LiPF_6$ vs Li, (b) 1M $LiClO_4$ vs Li, (c) 1M $NaClO_4$ vs Na and (d) alumina coated TiS_2 with $LiPF_6$ vs Li with 100 mA g^{-1} current density in potential range of (0.5-3.0 V).

Formation of a homogenous solid solution with intercalating ions is typically reflected via the observation of a smooth sloping voltage plateau in the discharge/charge profile. Sloping voltage plateau is observed with the Li^+ and Na^+ intercalation/de-intercalation phenomenon in TiS_2. Appearance of a small flat plateau in the 1st cycle suggests a 1st order phase transition. However, in view of the formation of solid solutions, 1st order phase transition can be ruled out here. The presence of plateau region around 0.7 V is due to the formation of a facile and stable solid electrolyte interphase (SEI) at the electrode surface, which remains intact in the subsequent cycles. The plateau is observed to be more

prominent in the 1st cycle for the alumina coated TiS_2 sample with the $LiPF_6$ based electrolyte. In this case the SEI layer is very pronounced which may due to the porous nature of the alumina coating on the TiS_2. The porous nature of the alumina coating allows the breathing space for the intrinsic structure following the intercalation of ions. The characteristic plateau is obtained as well for the uncoated sample for Li^+ intercalation **Figure** 9a and **Figure** 9d. With regard to the Na-ion intercalation, irreversible loss in capacity is much less compared to the Li^+ counterparts. This suggests that the presumed SEI formation for a Na^+-ion intercalation, irreversible loss in capacity is much less compared to that of an Li^+ counterparts. This suggests that the presumed SEI formation for a Na^+-ion based system is less compared to that of a Li^+-ion-based intercalation chemistry.

For all samples, the initial specific capacity obtained are much higher than the reported values. Studies were done on MoS_2 samples prepared by the same ALD technique; capacity higher than the theoretical values were reported.[11] This was attributed to the activation of more surface adsorption sites with reversible interaction with the alkali-ion leading to higher charge/energy storage. Here, we kept the lower potential limit to 0.5 V so as to completely eliminate the contributions from conversion reaction. With $LiPF_6$ based electrolyte **Figure** 9a, the 1st cycle charge capacity is more suggesting increased oxidation of electrolyte at the TiS_2 surface and hence SEI formation at the TiS_2 electrode will be feasible. For $LiClO_4$ based electrolyte, the first cycle discharge capacity is the highest. However, a higher irreversible capacity loss is observed which can be assigned to the higher salt decomposition and probably a thicker SEI.

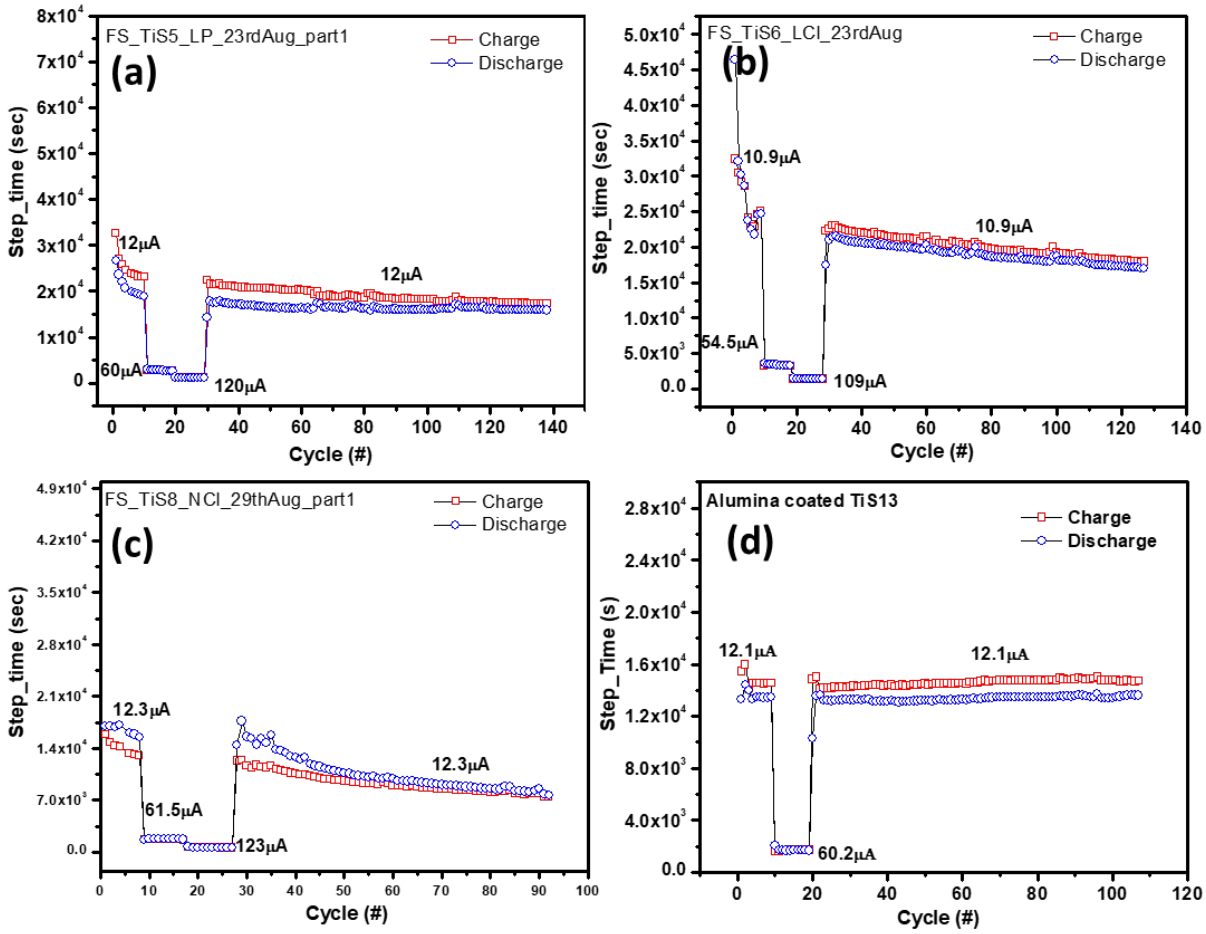

Figure 10: Rate capability and long term cyclability of TiS_2 with (a) 1M $LiPF_6$ in EC:DMC vs Li, (b) 1M $LiClO_4$ in EC:DMC vs Li, (c) 1M $NaClO_4$ in EC:DMC vs Na and (d) alumina coated TiS_2 with $LiPF_6$ in EC:DMC vs Li.

The discharge-charge cycling behavior at different current values has also been performed. It is observed that the efficiency of discharge - charge cycles at slower current rate is less as compared to the high current rate values **Figure** 10.The cells, however, could not be run at higher current values, this can be accounted on the fact that the thin films employed here have active materials in micrograms range. Another deciding factor could be the dense nature of obtained electrode as observed from the SEM images, where fast ion intercalation of alkali ions is not realizable. On decreasing back to the initial lower current values, the capacity values could be retraced back.

Conclusions

TiS_2 thin films having nanowall network morphology have been grown by ALD on various substrates. The nanowall network is crystalline in nature on c-sapphire and morphology is independent of underlying substrate. The network morphology exhibits high surface to volume ratio and shows excellent battery characteristics. This kind of morphology, may emerge as model electrode for other batteries chemistry.

References

[1] T. Suntola, J. Antson, inventors, Method for producing compound thin films, Patent 4058430, November 15, 1977.

[2] H. Kim, H. B. R. Lee, W.-J. Maeng, *Thin Solid Films* **2009**, *517*, 2563.

[3] R. W. Johnson, A. Hultqvist, S. F. Bent, *Materials Today* **2014**, *17*, 236.

[4] S. M. George, *Chemical Reviews* **2010**, *110*, 111.

[5] M. Leskelä, M. Ritala, *Angewandte Chemie International Edition* **2003**, *42*, 5548.

[6] R. L. Puurunen, *Chemical Vapor Deposition* **2014**, *20*, 332.

[7] R. L. Puurunen, *Journal of Applied Physics* **2005**, *97*, 121301.

[8] F. Grillo, J. A. Moulijn, M. T. Kreutzer, J. R. van Ommen, *Catalysis Today* **2018**, *316*, 51.

[9] C. Detavernier, J. Dendooven, S. Pulinthanathu Sree, K. F. Ludwig, J. A. Martens, *Chemical Society Reviews* **2011**, *40*, 5242.

[10] M. Ritala, J. Niinistö, *Chemical Vapour Deposition*; Royal Society of Chemistry; **2009**, 158.

[11] M. B. Sreedhara, S. Gope, B. Vishal, R. Datta, A. J. Bhattacharyya, C. N. R. Rao, *Journal of Materials Chemistry A* **2018**, *6*, 2302.

[12] L. Ma, R. B. Nuwayhid, T. Wu, Y. Lei, K. Amine, J. Lu, *Advanced Materials Interfaces* **2016**, *3*, 1600564.

[13] N. P. Dasgupta, X. Meng, J. W. Elam, A. B. F. Martinson, *Accounts of Chemical Research* **2015**, *48*, 341.

[14] H. Kasai, K. Tolborg, M. Sist, J. Zhang, V. R. Hathwar, M. Ø. Filsø, S. Cenedese, K. Sugimoto, J. Overgaard, E. Nishibori, B. B. Iversen, *Nature Materials* **2018**, *17*, 249.

[15] V. Pore, M. Ritala, M. Leskelä, *Chemical Vapor Deposition* **2007**, *13*, 163.

[16] N. Mahuli, S. K. Sarkar, *J. Vac. Sci. Technol. A* **2015**, *33*, 01A150.

[17] R. P. Abendroth, *Materials science and Engineering, University of Missouri, ANN Arbor, Michigan* **1957**, 114.

[18] M. S. Whittingham, *Science* **1976**, *192*, 1126.

[19] S. J. Sandoval, X. K. Chen, J. C. Irwin, *Physical Review B* **1992**, *45*, 14347.

[20] L. Zhang, D. Sun, J. Kang, H.-T. Wang, S.-H. Hsieh, W.-F. Pong, H. A. Bechtel, J. Feng, L.-W. Wang, E. J. Cairns, J. Guo, *Nano Letters* **2018**, *18*, 4506.

[21] W.D. Li, C.-Y. Xu, Y. Du, H.-T. Fang, Y.-J. Feng, L. Zhen, *Journal of The Electrochemical Society* **2013**, *161*, A75.